

# **Thin Film Chirality Measurements Via Cavity Ring-down Polarimetry**

**Alexandros K.Spiliotis**

**Optoelectronics-Nanoelectronics Master Course,  
Department of Physics, Univeristy of Crete**

# Table of Contents

<b>1.INTRODUCTION.....</b>	<b>IV</b>
<b>2. PROPAGATION OF LIGHT IN CHIRAL AND ACHIRAL MATERIALS-FRESNEL COEFFICIENTS.....</b>	<b>1</b>
<u>2.1</u> .INTRODUCTION.....	1
<u>2.2</u> .REFRACTION OF LIGHT.....	1
<u>2.3</u> .FRESNEL EQUATIONS.....	4
<u>2.4</u> .REFLECTION FROM A CHIRAL-ACHIRAL INTERFACE.....	8
<u>2.5</u> .PROPAGATION IN A CHIRAL MEDIUM.....	13
<u>2.6</u> .PROPAGATION OF LIGHT INSIDE A CHIRAL SLAB.....	16
<u>2.7</u> .MODE AND PHASE MATRICES.....	17
<u>2.8</u> .EVANESCENT WAVE AND GOOS-HÄNCHEN EFFECT.....	20
<b>3.OPTICAL CAVITY RING-DOWN TECHNIQUES.....</b>	<b>26</b>
<u>3.1</u> .INTRODUCTION.....	26
<u>3.2</u> .CAVITY RING-DOWN SPECTROSCOPY (CRDS).....	26
<u>3.3</u> .CAVITY RING-DOWN ELLIPSOMETRY (CRDE).....	28
<u>3.4</u> .EVANESCENT WAVE CAVITY RING-DOWN ELLIPSOMETRY(EW-CRDE).....	29
<u>3.5</u> .CHIRAL CRD.....	33
<u>3.6</u> .OTHER TYPES OF RUNNING CAVITIES.....	35
<b>4. EVANESCENT-WAVE CHIRAL SENSING VIA SIGNAL REVERSING CAVITY- ENHANCED POLARIMETRY.....</b>	<b>36</b>
<u>4.1</u> . INTRODUCTION.....	36
<u>4.1.1</u> . <i>Experimental setup</i> .....	36
<u>4.1.2</u> . <i>Derivation of the optical rotation measurement formula</i> .....	38
<u>4.1.3</u> . <i>Experimental process-Results</i> .....	40
<u>4.1.4</u> . <i>Discussion of the results</i> .....	42
<b>5.CHIRALITY MEASUREMENT IN THIN FILMS.....</b>	<b>42</b>
<u>5.1</u> .INTRODUCTION.....	42
<u>5.2</u> .OPTICALLY ACTIVE FABRY-PEROT INTERFEROMETER.....	44
<u>5.3</u> .SIMULATIONS.....	46
<u>5.4</u> . EXPERIMENT PROPOSAL.....	55
<b>6.BIBLIOGRAPHY.....</b>	<b>56</b>
<b>7.APPENDIX-REFLECTION COEFFICIENTS.....</b>	<b>57</b>

## Acknowledgments

I am grateful to my thesis advisor, Dr Peter T. Rakitzis, for his support and guidance throughout the two years I have already spent in his research team, and for giving me the chance to work in this team, which resulted in the production of this thesis, as well as my great development as a physicist.

I also have to thank Dr Benoit Loppinet, who aided much in producing this thesis, by guiding me through producing the theoretical work presented in the last chapter.

I would like to thank the two post-doctoral researchers of the team, Dr George Katsoprinakis and Dr Dimitris Sofikitis, who aided me a lot with writing this thesis, and from whom I learnt a lot throughout these two years.

Thanks to my colleagues, Dr Lykourgos Bougas, past grad student and Katerina Stamataki, current grad student, for our great collaboration as members of the team.

A great thank you to my parents, Rebecca and Kostas, for their invaluable support of all kinds, all over the years.

# 1. Introduction

Chirality is an intrinsic property of objects which is encountered in many branches of science. The general description of this phenomenon is the inequality of an object to its mirror image. A familiar example of a chiral object is the hand, where the name of the phenomenon is derived from (greek: χεῖρ). When one hand is put above the other with opposite sides facing, the features of one hand do not match with the features of the other. This means that each hand is not a superimposable image of the other. A chiral object and its mirror image are called enantiomorphs, and when referring to molecules, enantiomers. Sugars are other examples of chiral substances, the two enantiomers of which have distinguishable properties from each other. For example, the sugar that is widely used as a sweetener is D-Glucose, the right-handed enantiomer of Glucose; L-Glucose, the left-handed correspondent, is not naturally occurring, does not taste sweet and also, cannot be used by living organisms as a source of energy, as D-Glucose is.

Chiral molecules display an interesting property when interacting with light: the polarization of the wave is rotated at the direction of the molecule's handedness. That is, when a plane wave propagates through a medium of right helicity, its plane of polarization is rotated to the right (considering the light frame), no matter which side it enters the medium (fig. 1a). This is called the chiral or optical rotation of light, which is contrary to the Faraday rotation, where the rotation, considering the light frame,

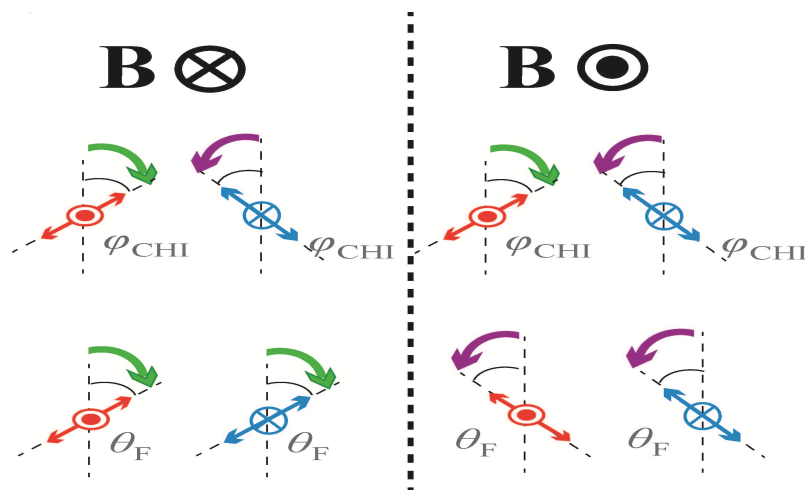


Figure 1: Chiral rotation (a) and Faraday rotation (b) in the lab frame, for the corresponding positive and negative magnetic fields

depends on the side of the medium on which the light enters (fig. 1b). These two symmetries are explained in more details later.

But where does this optical rotation come from? In section 2.5, a mathematical

approach is taken, starting from Maxwell's equations, to explain what happens when a light wave propagates through a chiral medium. For a more qualitative explanation, the circular birefringence and circular dichroism effects are to be taken into account. Any linear polarized light wave can be considered as the superposition of two circularly polarized waves, one left- and one right-circularly polarised. Circular birefringence is an intrinsic property of chiral media, which dictates that each circularly polarized component propagates with different speed inside the medium. This means that a chiral medium has two effective refractive indices,  $n_R$  and  $n_L$ , one for each wave component. The different refractive indices result in a phase difference between the two circularly polarized waves, which is translated into a rotation of the polarization plane (see figure 2). The strength of the chirality effect is determined by the difference of the refractive indices, given by the chirality factor  $\gamma$  ( $\gamma=n_R-n_L$ ).

Optical rotation is the dispersive property of the chiral medium, related to the corresponding absorptive property, circular dichroism. Circular dichroism is the difference in the absorbance of left ( $A_L$ ) and right ( $A_R$ ) circularly polarized light by a chiral medium. It only occurs at wavelengths where a chiral medium absorbs light, and is connected to optical rotation via the Kramers-Kronig relations (figure 2). Circular dichroism is a measurable quantity itself, and is used in studying proteins and other biological molecules. In a circular dichroism measurement experiment, left and right circularly polarized light is inserted in a chiral medium, and the difference of absorption in the output is measured. This difference is wavelength- dependent, as is the optical rotation. The measurement of circular dichroism is one of the future

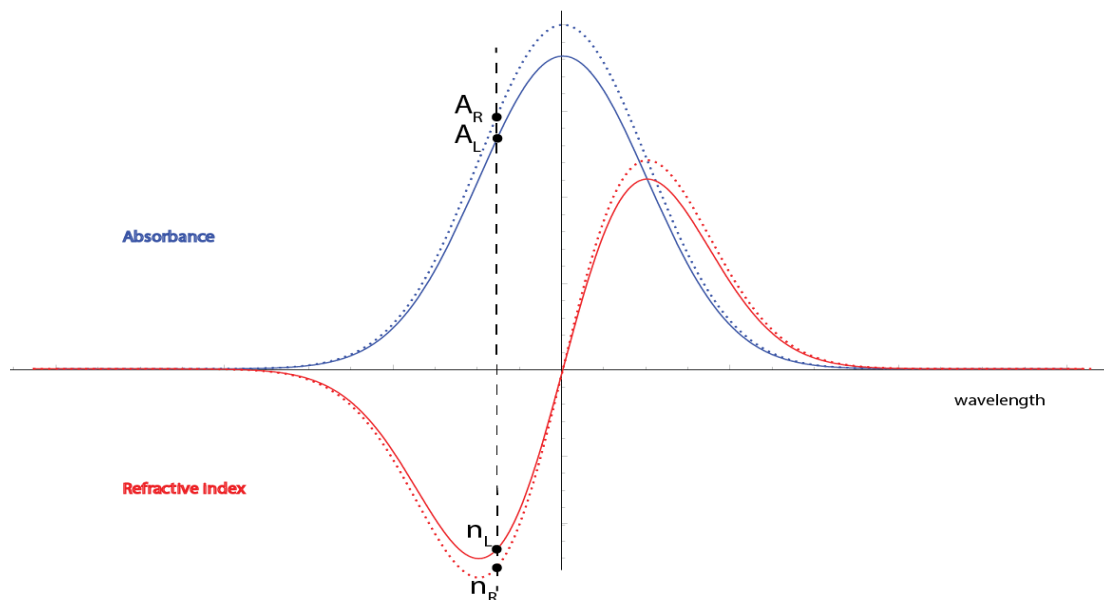


*Figure 2: Circular birefringence and circular dichroism on a chiral medium. For a given wavelength, there are two absorbances and refractive indices, one for each circular polarization.*

prospects of the technique presented in this work.

The measurement of chirality is of great importance to many fields, from

pharmacology to chemistry and fundamental physics. Chiral sensing of weak signals is difficult, because of the high, time-dependent backgrounds (e.g. spurious birefringence) that suppress them and the imperfect and slow subtraction procedures used up to now. Recently, Bougas et al.<sup>[1]</sup> proposed a new technique for measuring weak chiral signals, using signal reversals in an EW-CRDE configuration with counter-propagating beams. The aforementioned problems can all be solved by this technique: as we saw before, the weak signal can be enhanced by the number of intracavity round-trips; spurious linear birefringence is suppressed, by a Faraday rotation; and a rapid reversal procedure is accomplished by reversing the Faraday rotation, by rotating the magnetic field direction, and then reversing the signals obtained from the counter-propagating beams. This way, measurement of the chirality of gaseous and liquid chiral samples can be feasible. This technique is examined in more depth in paragraph 3.5.

The technique introduced by Bougas et al., and applied for chiral sensing by Sofikitis et al.<sup>[2]</sup> gives a great advantage in measuring very small quantities of a chiral sample. Only a few millibars of a gaseous chiral sample and a few milliliters of a liquid chiral sample are enough to measure the chirality effect strength with a precision in the order of  $10^{-6}$ . Such a sensitive measurement can prove very useful in fields like pharmacology, where small sample volumes are better to be used. A possible application could be the determination of a medicine's content of the two chiral enantiomers. In most cases, the two enantiomers have different properties, e.g. one of them is a beneficial enantiomer whilst the other is neutral, or even harmful. Such quality control is important in drug design, synthesis and production.

This technique, being based on Total Internal Reflection (TIR) at the interface between a prism and the sample, is functional up to a certain sample refractive index; if index matching between the prism and the sample occurs, TIR conditions are not met, and the light is transmitted through the sample, making the measurement impossible. In the last part of this work, the same configuration is used to propose a way to measure samples of even smaller volume, with refractive indices larger than the one of the prism. The sample used is a thin film, and the technique is based on the waveguiding effect; the light is trapped inside the sample, making multiple reflections back and forth, thus maintaining TIR conditions between the sample and the air. The light energy travels back to the prism and continues travelling through the cavity, with its plane of polarization rotated owing to the chirality effect of the sample. The sample in this configuration can be seen as an optically active Fabry-Perot etalon, which was previously theoretically studied by Lalov and Miteva<sup>[3]</sup>, Lalov and Georgieva<sup>[4]</sup> and Silvermann and Badoz<sup>[5]</sup>. Lastly, a possible experimental process is proposed to examine the capability of the proposed configuration to measure the chirality factor  $\gamma$  of a thin chiral film.

We consider the two experimental processes presented in this work to be complementary to each other. While the configuration introduced by Sofikitis et al. is proposed for the measurement of samples with lower refractive indices than the one of

## Introduction

the prism, the one presented in this work covers the refractive indices equal to or higher than that of the prism. Therefore, any liquid chiral sample can be measured by the configurations proposed in this work, using only a very small volume of the substance to be measured. The choice whether “bulk” material or a thin film is to be used, should be made based on the refractive index of the sample.

## 2. Propagation of light in chiral and achiral materials

### 2.1. Introduction

In this section, we make a general discussion about the propagation of light through chiral-achiral media configurations. To analyze the light propagation in this case, one can start from the Maxwell equations, then derive the relations that describe light propagation in the simple case of an achiral material. We will derive these equations, known as Fresnel coefficients, for reflection and transmission, and use them to describe the refraction of light in an achiral medium. Then, introducing the correction for a chiral material in the Maxwell equations, we study the reflection from a chiral-achiral interface, extracting the corresponding generalized Fresnel equations. Following this, we show how the light propagates in a chiral medium, after refraction at the interface with an achiral medium, taking into account two cases, that of an infinite chiral medium and that of a chiral slab between two achiral media. Finally, a discussion about the evanescent wave and Goos-Hänchen is made, effects that take place in Total Internal Reflection conditions.

### 2.2. Refraction of light

We first consider an isotropic, nonconducting, non-chiral medium, with electric permittivity  $\epsilon$  and magnetic permeability  $\mu$ . The electric field  $E$  and magnetic field  $H$  are related via the well-known Maxwell Equations,

$$c \nabla \times E = -\frac{\partial B}{\partial t} \quad (2.2.1)$$

$$\nabla \times H = \frac{\partial D}{\partial t} \quad (2.2.2)$$

$$\nabla \cdot H = 0 \quad (2.2.3)$$

$$\nabla \cdot E = 0 \quad (2.2.4)$$



## Propagation of light in chiral and achiral materials

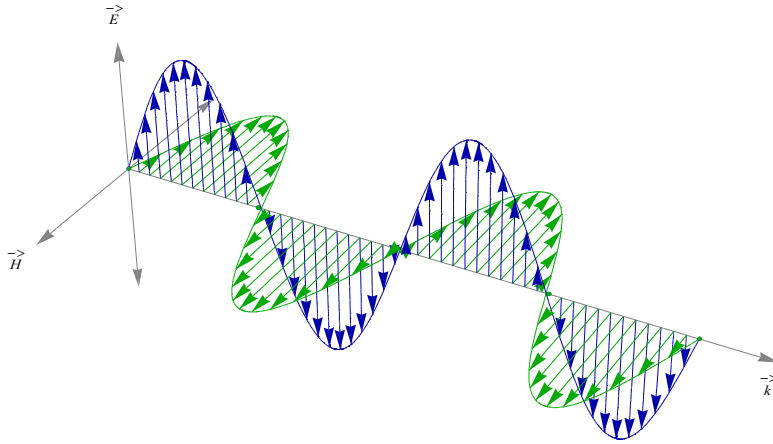


Figure 3: Propagation of a TEM electromagnetic field

Where  $\mathbf{D}=\epsilon\mathbf{E}$  the electric displacement field and  $\mathbf{B}=\mu\mathbf{H}$  the magnetic field. The equations used for the study of a chiral medium are similar, only with slightly different relations for  $\mathbf{D}$  and  $\mathbf{B}$

For a plane harmonic wave, these formulae can give a simplified expression for the magnitudes of the two fields. The solution of the basic wave equation:

$$\nabla^2 U = \frac{1}{u^2} \frac{\partial^2 U}{\partial t^2} \quad (2.2.5)$$

would then be

$$e^{i(\mathbf{k}\cdot\mathbf{r}-\omega t)} \quad (2.2.6)$$

Where  $\mathbf{k}$  is the wavevector,  $\mathbf{r}$  is the space vector  $\sqrt{x^2+y^2+z^2}$ ,  $\omega$  is the wave frequency, related to  $\mathbf{k}$  by  $\omega=\mathbf{k}c/n$ . We now have to simplify the del operator and the time derivative from the Maxwell equations. So, first we take the del operator

$$\nabla = \hat{i} \frac{\partial}{\partial x} + \hat{j} \frac{\partial}{\partial y} + \hat{k} \frac{\partial}{\partial z} \quad (2.2.7)$$

of the wave expression (2.2.6):

$$\nabla e^{i(\mathbf{k}\cdot\mathbf{r}-\omega t)} = i\mathbf{k} e^{i(\mathbf{k}\cdot\mathbf{r}-\omega t)} \quad (2.2.8)$$

and then its time derivative:

$$\frac{\partial}{\partial t} e^{i(\mathbf{k}\cdot\mathbf{r}-\omega t)} = -i\omega e^{i(\mathbf{k}\cdot\mathbf{r}-\omega t)} \quad (2.2.9)$$

to find that we could substitute those operators at (2.2.1 - 2.2.4) as such:

$$\frac{\partial}{\partial t} \rightarrow -i\omega$$

$$\nabla \rightarrow i\mathbf{k}$$

By substituting the expressions for D and H, we have

$$\mathbf{k} \times \mathbf{E} = \mu\omega \mathbf{H} \quad (2.2.10)$$

$$\mathbf{k} \times \mathbf{H} = -\varepsilon\omega \mathbf{E} \quad (2.2.11)$$

$$\mathbf{k} \cdot \mathbf{E} = 0 \quad (2.2.12)$$

$$\mathbf{k} \cdot \mathbf{H} = 0 \quad (2.2.13)$$

Taking a look to these relations, one can see that  $\mathbf{k}$ , the vector of the wave propagation, is perpendicular to both fields, which in turn are perpendicular to each other (Figure 3), which is an expected result. What needs to be extracted is a convenient relation between the magnitudes of the two fields. This can be obtained easily from (2.2.11)

$$\mathbf{H} = \frac{\varepsilon\omega}{k} \mathbf{E} \quad (2.2.14)$$

This relation will be useful for the study of how the wave propagates through the presence of an interface between two media of different refractive index. Consider a plane light beam propagating through an isotropic, nonconducting medium of refractive index  $n_1$ , towards the boundary with another medium of refractive index  $n_2$ . Part of the wave will be reflected, and another part will be transmitted into the second medium, as shown in [Figure 4](#).

## Propagation of light in chiral and achiral materials

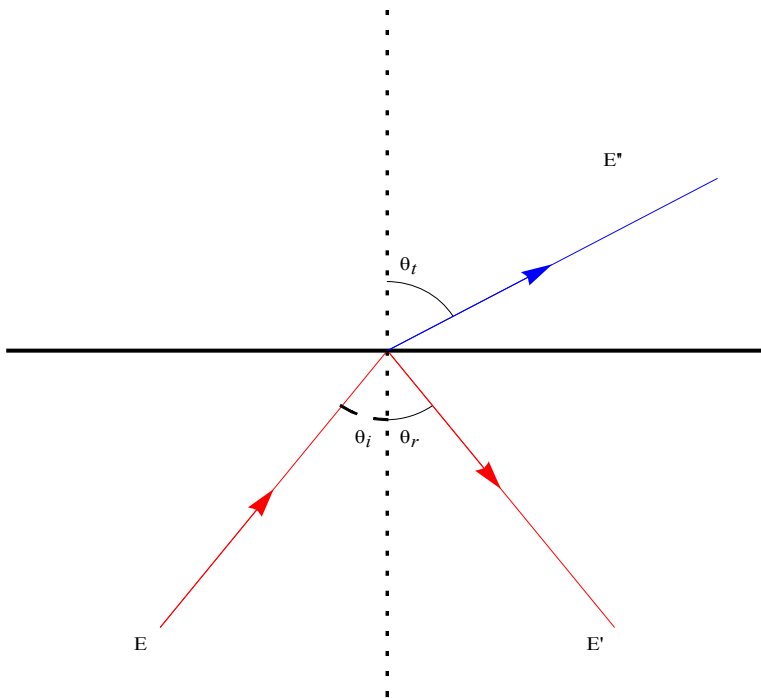



Figure 4: Refraction of a wave. The wavefunction should be continuous at the interface between the two media.

Let  $\mathbf{k}, \mathbf{k}', \mathbf{k}''$  denote the wavevector of the incident, reflected and transmitted wave respectively. From the plane wave expression (2.2.6), we have the following expressions for the three waves:

$$\begin{aligned} E &= \exp[i(\mathbf{k} \cdot \mathbf{r}) - \omega t] \\ E' &= \exp[i(\mathbf{k}' \cdot \mathbf{r}') - \omega t] \\ E'' &= \exp[i(\mathbf{k}'' \cdot \mathbf{r}'') - \omega t] \end{aligned} \quad (2.2.15)$$

 Snell's law is in effect for all three waves simultaneously, and can be derived by the boundary conditions, i.e. that the wave arguments should be equal at the boundary, so

$$n_1 \sin \theta_1 = n_2 \sin \theta_2 \quad (2.2.16)$$

### 2.3. Fresnel Equations

We now return to the simplified equations (2.10)-(2.13). Let  $\mathbf{E}, \mathbf{E}', \mathbf{E}''$  denote the

electric field amplitudes of the incident, reflected and transmitted wave respectively. The corresponding magnetic fields will be:

$$\mathbf{H} = \frac{1}{\mu\omega} \mathbf{k} \times \mathbf{E} \quad (2.3.1)$$

$$\mathbf{H}' = \frac{1}{\mu\omega} \mathbf{k}' \times \mathbf{E}' \quad (2.3.2)$$

$$\mathbf{H}'' = \frac{1}{\mu\omega} \mathbf{k}'' \times \mathbf{E}'' \quad (2.3.3)$$

From these relations, we can extract the reflection and transmission amplitudes after the incidence at the interface between the two media. The reflection and transmission will depend on what the polarization of the incident wave will be. Considering that, we will obtain the corresponding amplitudes for both the case of incident s (E parallel to the boundary) and p (E perpendicular to the boundary) polarization.

The boundary conditions for a plane wave will lead us to the solution for the reflection and transmission coefficients. It is required that the tangential components of the two fields be continuous at the upper and lower side of the interface. From this, we obtain

$$E' + E = E'' \quad (2.3.4)$$

$$-H \cos\theta + H' \cos\theta = -H'' \cos\varphi \quad (2.3.5)$$

$$-kE \cos\theta + k' E' \cos\theta = -k'' E'' \cos\varphi \quad (2.3.6)$$

for s polarization, and

$$H - H' = H'' \quad (2.3.7)$$

$$kE - k' E' = -k'' E'' \quad (2.3.8)$$

$$E \cos\theta + E' \cos\theta = E'' \cos\varphi \quad (2.3.9)$$

for p-polarization, with  $\varphi$  being the angle of the refracted beam in the second medium.

We now define the reflection coefficients,  $r_s$  and  $r_p$ , and the transmission coefficients,  $t_s$  and  $t_p$ , where the s and p subscripts denote that the coefficients are for s and p

polarization incident respectively:

$$r_s = [E'/E] |_s \quad (2.3.10)$$

$$r_p = [E''/E] |_p \quad (2.3.11)$$

$$t_s = [E''/E] |_s \quad (2.3.12)$$

$$t_p = [E''/E] |_p \quad (2.3.13)$$

Then, by eliminating  $E''$ , we obtain an expression for the reflection amplitudes:

$$r_s = \frac{n_1 \cos \theta - n_2 \cos \varphi}{n_1 \cos \theta + n_2 \cos \varphi} \quad (2.3.14)$$

$$r_p = \frac{n_2 \cos \theta - n_1 \cos \varphi}{n_1 \cos \theta + n_2 \cos \varphi} \quad (2.3.15)$$

and by eliminating  $E'$ , an expression for the transmission amplitudes:

$$t_s = \frac{2 \cos \theta \sin \varphi}{\sin(\theta - \varphi)} \quad (2.3.16)$$

$$t_p = \frac{2 \cos \theta \sin \varphi}{\sin(\theta - \varphi) \cos(\theta - \varphi)} \quad (2.3.17)$$

The above equations are known as the Fresnel equations. They are very useful in giving the intensity and phase of the reflected and transmitted waves which are produced by an incident wave at an interface between two media.

The total intensity of the reflected wave is given by the reflectance, i.e. the square of the absolute value of the reflection coefficient:

$$R_s = |r_s|^2 = \left| \frac{E'}{E} \right|^2 \quad (2.3.18)$$

$$R_p = |r_p|^2 = \left| \frac{E'}{E} \right|^2 \quad (2.3.19)$$

The reflectance is defined as the fraction of the energy of the incident wave that is reflected. Since energy is conserved after the boundary,

$$|r_s|^2 + |t_s|^2 = 1 \quad (2.3.20)$$

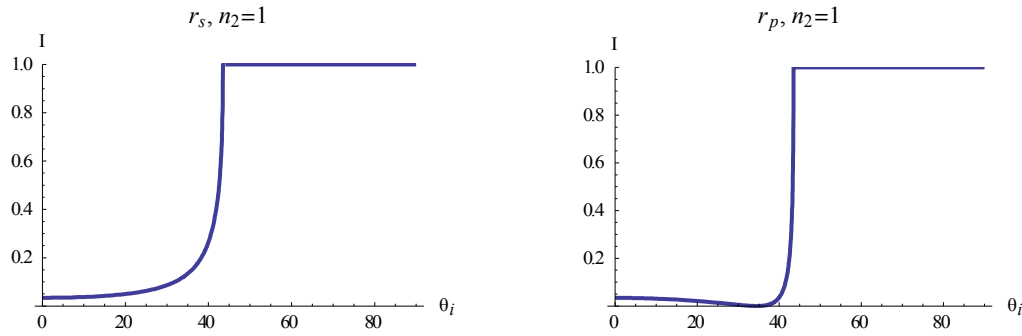


Figure 5: Reflectance for incident s- (a) and p-polarization (b)

Figure 5 shows how the reflectance varies with the angle of incidence of the wave, for a refractive index ratio  $\frac{n_1}{n_2} = 1.45$ . We can see that, after a certain value of the angle of incidence, called the critical angle, the reflectance is equal to 1. This means that the whole light beam is reflected at the interface, that is, we have Total Internal Reflection (TIR). This critical angle is given by Snell's law, by setting  $\theta_2 = 90^\circ$ :

$$\theta_c = \arcsin \frac{n_2}{n_1} \quad (2.3.21)$$

For TIR conditions, the Fresnel equations become:

$$r_s = -\frac{\cos\theta - i\sqrt{\sin^2\theta - n^2}}{\cos\theta + i\sqrt{\sin^2\theta - n^2}} \quad (2.3.22)$$

$$r_p = -\frac{n^2 \cos\theta + i\sqrt{\sin^2\theta - n^2}}{n^2 \cos\theta + i\sqrt{\sin^2\theta - n^2}} \quad (2.3.23)$$

where, using Snell's law ( $n_1 \sin\theta = n_2 \sin\phi$ ), the angle  $\phi$  is eliminated, by expressing it in

terms of  $\theta$ . The TIR conditions will be discussed in more depth later. Note that the value of  $R_p$  becomes zero at a certain, non-zero angle. For  $\frac{n_1}{n_2}=1.45$ , this angle is  $44.6^\circ$ , marking the Brewster angle, i.e. the angle in which the p-polarization component of the reflected wave becomes zero.

## 2.4. Reflection from a chiral-achiral interface

The discussion made earlier about the Maxwell equations and their application in the case of a plane wave incident on a boundary between two different media, is similar in the case of chiral media. In this case, we define two refractive indices,  $n_+$  and  $n_-$ , each one corresponding to the respective positive or negative helicity of the incident wave, with  $n_+ - n_- = \gamma$ . The difference is that, when treating a chiral medium, the electric displacement field and magnetic induction are corrected by a factor proportional to the strength of the chiral effect, which is expressed by  $\gamma$ . These corrections would be<sup>[6] 1</sup>:

$$\mathbf{D} = \epsilon \mathbf{E} - g \frac{\partial \mathbf{H}}{\partial t} \quad (2.4.1)$$

$$\mathbf{B} = \mu \mathbf{H} + g \frac{\partial \mathbf{E}}{\partial t} \quad (2.4.2)$$

and, for a monochromatic wave,

$$\mathbf{B} = \mu \mathbf{H} - i\gamma \mathbf{E} \quad (2.4.3)$$

$$\mathbf{D} = \epsilon \mathbf{E} - i\gamma \mathbf{H} \quad (2.4.4)$$

where  $\gamma = \omega g$ .

Consider an s-polarized, monochromatic wave incident to the interface between an achiral and an (infinite) chiral medium, like in figure 4. The wave is propagating inside the medium in the  $xz$  plane, i.e. the plane of incidence, at the  $x$  direction, whilst the boundary lies at the  $zy$  plane. Its wavevector would then be  $\mathbf{k}_1 = (K, 0, q_1)$ , and its electric field, given the magnitude is unity, is given by

$$\mathbf{E}_s = (0, 1, 0) e^{i(Kx + q_1z)} \quad (2.4.5)$$

---

1 Note that these expressions are not the only ones to be found in literature; The discussion about the different formulae given by other researches is made in [6]

Let  $\theta_1$  be the angle of incidence. The reflected wave will then be

$$E' = (r_{sp} \cos \theta_1, r_{ss}, r_{sp} \sin \theta_1) \exp^{i(Kx - q_1 z)} \quad (2.4.6)$$

The interesting element of this expression is the presence of non-zero x and z components of the electric field, since the incident wave only has a y component. This means that the reflected wave has its polarization plane changed, because of the interaction with the chiral medium at the interface. The  $r_{sp}$  coefficient gives the amplitude of this polarization change, i.e. the amplitude of the p-component of the polarization of the reflected wave, when the incident wave is s-polarized. We will later show that it is only present when the chiral effect is present; if  $\gamma=0$ ,  $r_{sp}=0$ .

The respective expressions for the reflected part of a p-polarization incident wave is:

$$E' = (r_{pp} \cos \theta_1, r_{ps}, r_{pp} \sin \theta_1) \exp^{i(Kx + q_1 z)} \quad (2.4.7)$$

and the corresponding transmission waves will be:

$$E''_s = (t_{sp} \cos \theta_2, t_{ss}, -t_{sp} \sin \theta_2) e^{i[Kx + q_2(z-d)]} \quad (2.4.8)$$

$$E''_p = (t_{pp} \cos \theta_2, t_{ps}, -t_{pp} \sin \theta_2) e^{i[Kx + q_2(z-d)]} \quad (2.4.9)$$

for s- and p-polarized incident waves, respectively.

In some cases, it is more convenient to use the helicity notation to express the reflection and transmission coefficients. That is, for example, the negative helicity component of a reflected wave, when the incidence wave is of positive helicity, is  $r_{+-}$ , and so forth. The derivation of the helicity-notated coefficients from their s-p notated equivalents is shown in the appendix. Here we give the reflection coefficients, as given by Lekner<sup>[6]</sup>.

Let

$$c_1 = \cos \theta_1, \quad c_{\pm} = \cos \theta_{\pm} = \sqrt{1 - (n_1 \sin \theta_1 / n_{\pm})^2}, \quad m = \sqrt{\frac{\varepsilon \mu_1}{\mu \varepsilon_1}} \quad (2.4.10)$$

Where  $\mu_1, \varepsilon_1$  are the permeability and permittivity of the medium of incidence, and  $\mu, \varepsilon$  are the respective quantities for the achiral medium. All reflection coefficients share a common denominator,



Propagation of light in chiral and achiral materials

$$D = c_1^2 + c_1(c_+ + c_-)(m - m^{-1})/2 + c_+c_- \quad (2.4.11)$$

Then the reflection coefficients for s-polarized light incident are<sup>[6]</sup>

$$r_{ss} = [c_1^2 + c_1(c_+ + c_-)(m - m^{-1})/2 + c_+c_-]/D \quad (2.4.12)$$

$$r_{sp} = -ic_1(c_+ - c_-)/D \quad (2.4.13)$$

And for p-polarized light incident,

$$r_{pp} = -[c_1^2 + c_1(c_+ + c_-)(m - m^{-1})/2 - c_+c_-]/D \quad (2.4.14)$$

$$r_{ps} = -ic_1(c_+ - c_-)/D \quad (2.4.15)$$

Note that  $r_{sp} = r_{ps}$ , and that these quantities are always zero for  $c_+ = c_- \Rightarrow \gamma = 0$ . Since the meaning of the  $r_{sp}$  coefficient is the quantity of the the amplitude alteration of s-polarization incident to p-polarization, one could conclude that, when  $r_{sp} = 0 = r_{ps}$ , there is no alteration in the polarization plane whatsoever, and the incident polarization is the same with the reflected. To show that this is not exactly the case here, an alternative notation can be used for the reflection amplitudes.

As is known, a plane polarization can be expressed in terms of circular polarization or helicity. Any wave of a plane polarization can be viewed as the coherent superposition of two waves of opposite helicities (+ and -) and equal amplitudes. Thus, the reflection amplitudes can be expressed in terms of the helicity too, instead of the planes of the polarization. For incident circularly polarized light, the reflection amplitudes  $r_{++}$ ,  $r_{+-}$ ,  $r_{-+}$ ,  $r_{--}$  are defined. For example, the  $r_{+-}$  amplitude is the complex amplitude of the light reflected with negative helicity, when light with positive helicity is incident.

The reflection amplitudes using the helicity notation can be expressed in terms of the corresponding plane polarization amplitudes<sup>[6]</sup>:

$$r_{++} = \frac{1}{2}(r_{ss} - r_{pp}) - \frac{1}{2}i(r_{sp} + r_{ps}) \quad (2.4.16)$$

$$r_{+-} = -\frac{1}{2}(r_{ss} + r_{pp}) - \frac{1}{2}i(r_{sp} - r_{ps}) \quad (2.4.17)$$

$$r_{-+} = -\frac{1}{2}(r_{ss} + r_{pp}) + \frac{1}{2}i(r_{sp} - r_{ps}) \quad (2.4.18)$$

$$r_{--} = \frac{1}{2}(r_{ss} - r_{pp}) + \frac{1}{2}i(r_{sp} + r_{ps}) \quad (2.4.19)$$

Figure 4 shows the reflectance of each helicity change, for  $n_1=1.45332$  and  $n=1$ , when  $\gamma=0.6*10^{-6}$ .  $r_{++}$  and  $r_{--}$  have a first peak exactly at the critical angle, but then a small slope occurs, until the reflectance goes back to 1 at grazing incidence. This slope is owing to the rise of  $r_{+-}$  and  $r_{-+}$  after the critical angle. This would mean that, when in TIR conditions, there is a change in the helicity of the light after the reflection, even if there is no chiral effect to change the polarization plane. The change in the helicity, though, is not a change in the polarization plane per se, but a change in the phase between the s and p polarization amplitudes. Even for angles smaller than the critical angle, there is a non-zero value for  $r_{-+}$  and  $r_{+-}$ . This non-zero value is attributed to the property of the light to change its helicity from positive to negative after the reflection at the surface. It is shown that the  $r_{+-}$  is 3%, and  $r_{++}$  is 0% up to  $40^\circ$ , so all the reflected light has its helicity completely changed.

The explanation of the non-zero values after the critical angle is somewhat different. The light polarization in TIR undergoes a phase shift between the s and p polarizations, when it is reflected at the surface, whether the medium it reflects from is chiral or achiral. There is thus an inherent ellipsometric phase shift occurring at the interface. This is attributed to the Goos-Hänchen effect<sup>[7]</sup>, which shows that the light travels at the interface between the two media for a very short length while totally reflected, and while travelling there it undergoes a phase shift. This effect is discussed in more details in paragraph 4.3.

*Figure 6: Reflectances vs angle of incidence, using the helicity notation. The sums  $r_{++}+r_{+-}$  and  $r_{-+}+r_{--}$  are equal to unity, at TIR conditions.*

Figure 7 shows the variation of the reflected wave energy vs the angle of incidence of the wave incident to the chiral-achiral boundary. The reflection coefficients are derived using the continuity of the tangential vector of the electric and magnetic fields at the boundary, as shown in the appendix. We can see that, for a strong chiral effect ( $\gamma \sim 10^{-3}$ ), the change in the plane of rotation is observable around the critical angle. This change is not observable using a more realistic number for  $\gamma$ , in the order of  $10^{-6}$ . Looking at the  $R_{ss}$  and  $R_{pp}$  plots of figure 7, one can see that the transition to unity magnitude is less steep than when the second medium is non-chiral. This is attributed to a non-zero  $R_{sp}$  coefficient exactly at the critical angle, which then drops exponentially to zero. This is in accordance with many studies, which have shown an enhancement of chirality effects in the vicinity of the critical angle. As we will see, our work will focus in that area, because the experimental configuration we use strongly favors searching at that vicinity.

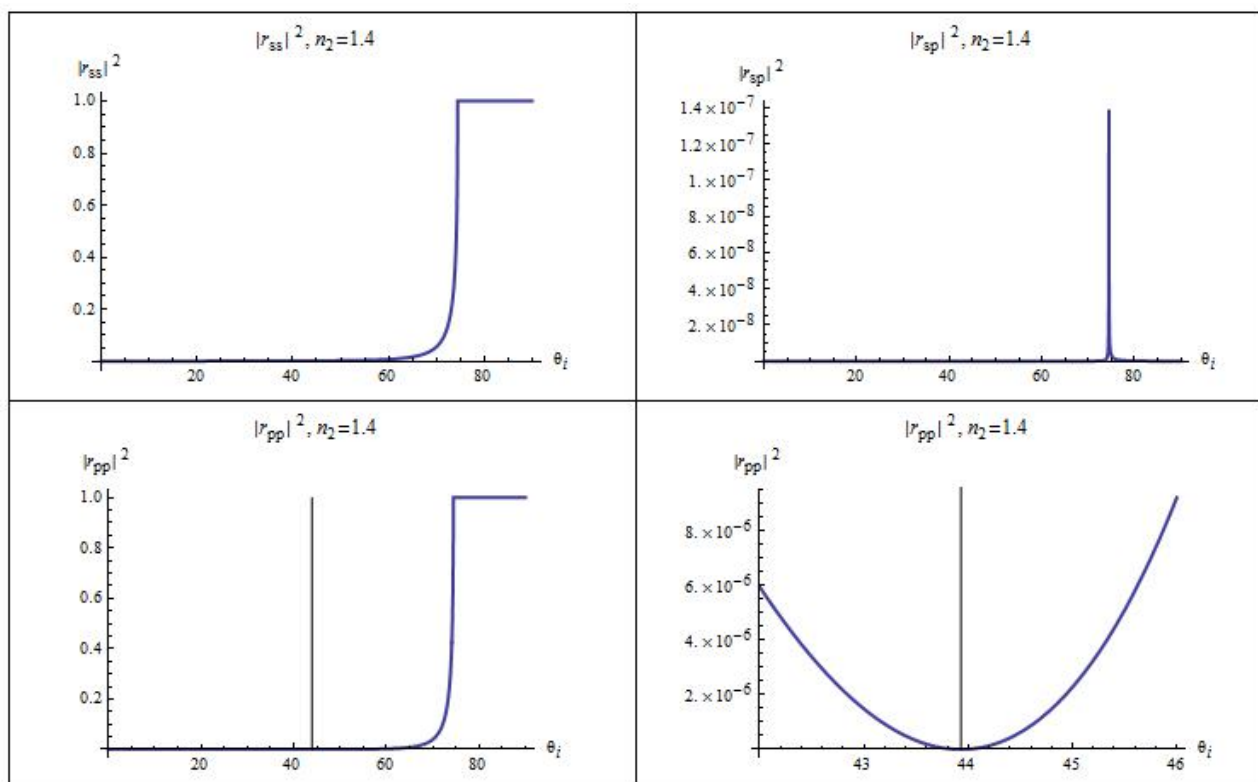


Figure 7: Reflection amplitudes from a chiral-achiral interface, where, for (a) incident s, reflected s polarization (b) incident s-, reflected p-polarization. Note that this amplitude is non-zero only in the vicinity of the critical angle (c) incident p-, reflected p-polarization (d) same as (c), but with a closer look at the angles in the vicinity of the Brewster angle ( $\sim 43.8^\circ$ )

## 2.5. Propagation in a chiral medium

Here we discuss the propagation of the light beam inside the chiral medium. Consider a

homogeneous chiral medium, with  $\epsilon, \mu$  and  $\gamma$  constant. Using the aforementioned expressions for  $\mathbf{D}$  and  $\mathbf{B}$  (2.2.1 - 2.2.4) and the variation of Maxwell equations, considering a time dependence of  $e^{-i\omega t}$ ,

$$\nabla \times \mathbf{E} = i\omega \mathbf{B} \quad (2.5.1)$$

$$\nabla \times \mathbf{H} = -i\omega \mathbf{D} \quad (2.5.2)$$

After some calculations (see appendix), we obtain three differential equations for the three E directional components

$$[(\epsilon\mu - \gamma^2) \frac{\omega^2}{c^2} - q^2] E_x - 2i \frac{\omega}{c} \gamma q E_y + q K E_z = 0 \quad (2.5.3)$$

$$2i \frac{\omega}{c} \gamma q E_x + [(\epsilon\mu - \gamma^2) \frac{\omega^2}{c^2} - K^2 - q^2] E_y - 2i \frac{\omega}{c} \gamma K E_z = 0 \quad (2.5.4)$$

$$K q E_x - 2i \frac{\omega}{c} \gamma K E_y + [(\epsilon\mu - \gamma^2) \frac{\omega^2}{c^2} - K^2] E_z = 0 \quad (2.5.5)$$

Since the three components are linearly independent, the determinant of their respective coefficients should be zero, i.e.

$$\begin{pmatrix} k_y^2 - q^2 & -2i\omega\gamma/c & Kq \\ 2iq\omega\gamma/c & k_y^2 - K^2 - q^2 & 2iK\omega\gamma/c \\ Kq & 2iK\omega\gamma/c & k^2 - K^2 \end{pmatrix} \quad (2.5.6)$$

where

$$k_y^2 = (\epsilon\mu - \gamma^2) \frac{\omega^2}{c^2} \quad (2.5.7)$$

and  $K$  is the x component of the wavevector. Note that  $K$  is the constant of motion, due to translational invariance in the x direction<sup>2</sup>.

From there, we see that  $q$  has 4 possible solutions; two for positive  $K$  (=propagation in the +z direction) and two for negative  $K$  (=propagation in the -z direction). Each one

## Propagation of light in chiral and achiral materials

of the two distinct eigenvalues of  $q$  for each  $K$  are corresponding to each one of the refractive indices of the chiral medium. A picture of this is given in figure 8.

Thus the wavevector is given by

$$k_{\pm} = \sqrt{K^2 + q_{\pm}^2} = n_{\pm} \frac{\omega}{c} = \sqrt{\epsilon\mu \pm \gamma} \frac{\omega}{c} \quad (2.5.8)$$

with  $\sqrt{\epsilon\mu \pm \gamma}$  being the two effective refractive indices of the medium.

As such, there will be two electric fields propagating inside the chiral medium:

$$E_+ \propto (q_+, ik_+, -K) \quad (2.5.9)$$

$$E_- \propto (q_-, -ik_-, -K) \quad (2.5.10)$$

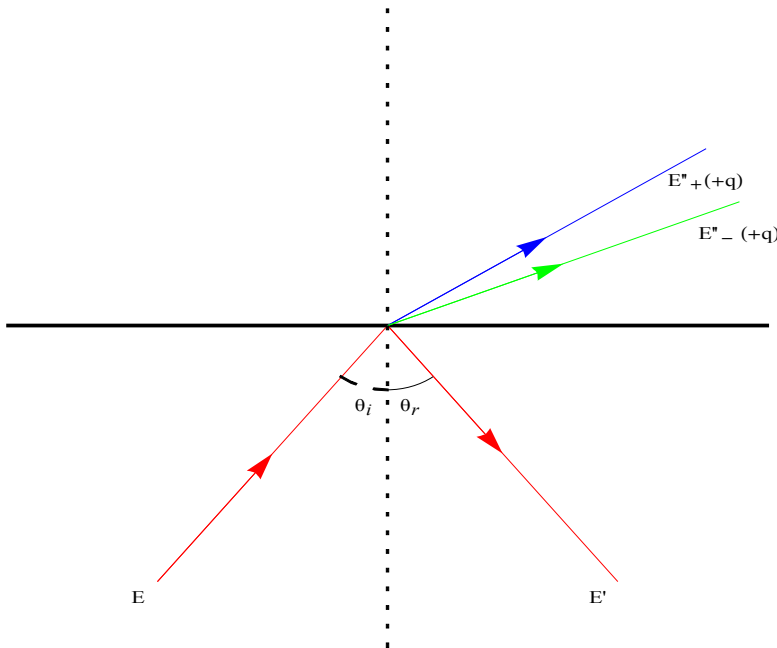


Figure 8: Refraction in a chiral medium

Practically, this means that, a plane polarized light beam is split in two beams, with different angles of refraction, when it enters a chiral medium, one with left and another with right circular polarization. This is an expected result, predicted by Fresnel in the 1820's, and experimentally demonstrated by Ghosh and Fisher<sup>[8]</sup> only in 2006. The physical explanation for this splitting lies into the existence of two refractive indices in

the chiral medium. As known, the refraction in a medium is a result of Fermat's theorem, which states that when light travels through two points, it will always travel in the path that will take the least time. The velocity of the light depends on the refractive index of the medium inside which it propagates, so when the light enters a chiral medium, it can travel under the effect of any of the refractive indices. As noted before, a plane polarized wave can be viewed as the coherent superposition of two circular polarized waves of equal amplitude ratio between them. So, when a beam of such polarization enters a chiral medium, the (+)-polarized portion of the wave will be refracted with a refractive index  $n_+$  and the (-)-polarized portion will be refracted with  $n_-$ . Thus each wave acquires a different phase as it propagates through the chiral medium.

### 2.6. Propagation of light inside a chiral slab

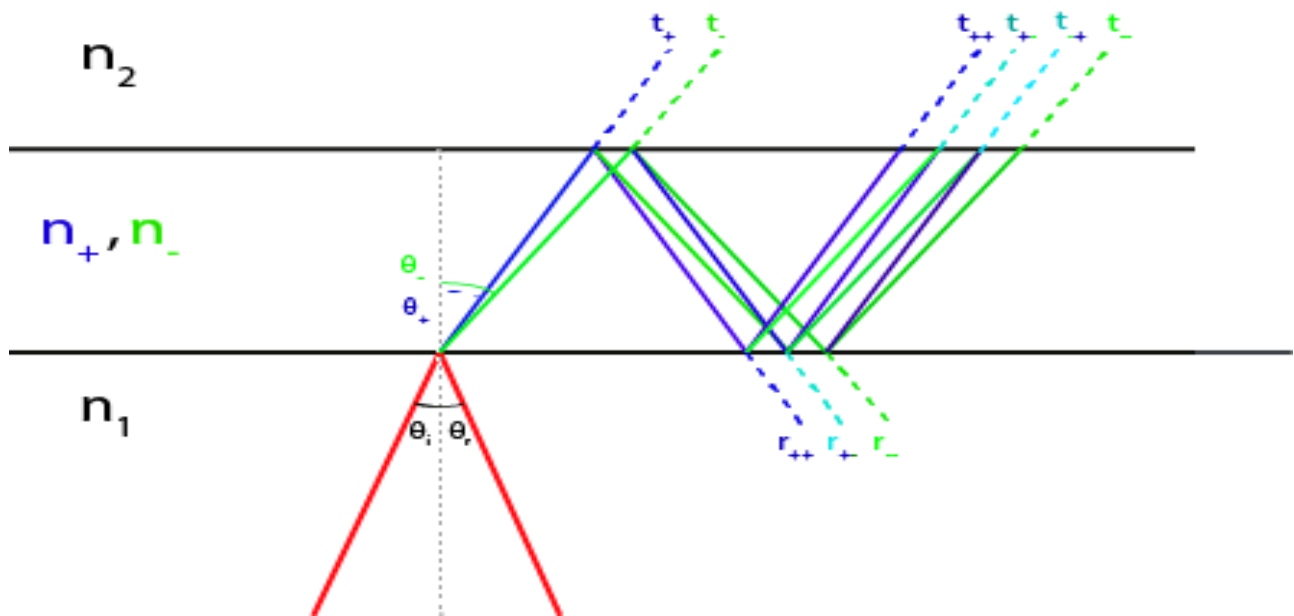


Figure 9: Propagation of a beam inside a chiral slab, assuming  $n_2 < n < n_1$

Consider a chiral layer of thickness  $d$  and infinite width<sup>3</sup>, between two achiral media of refractive indices  $n_1 = \sqrt{\epsilon\mu_1}$  and  $n_2 = \sqrt{\epsilon\mu_2}$  respectively. We will henceforth name the medium  $n_1$ , medium of incidence, and the medium  $n_2$  will be the substrate. The chiral medium has two refractive indices,  $n_{\pm} = \sqrt{\epsilon\mu \pm \gamma}$ , as noted before, each

<sup>3</sup> We can make this approximation if we consider the wavelength of the light propagating through the chiral slab to be small, compared to the slab thickness.

applying to each circular polarization, and it lays between  $z=0$  and  $z=d$ . When not in TIR conditions, the light propagates inside the medium at the forward  $z$  direction, split in two beams, as we saw in chapter 2.2. When the two beams encounter the slab-substrate interface, the snell's law is in effect again, and there will be another reflected-transmitted pair from this interface. Each reflected beam will again split in two reflected beams upon reflection, each one of pure right or left circular polarization. The angle of incidence of each beam at the  $z=d$  interface is the angle  $\theta_{\pm}$ , applying for the respective polarization of each beam. This will also be the angle of every incident-reflected pair inside the chiral slab for any more reflections occurring. So Snell's law gives

$$n_2 \sin \theta_2 = n_{\pm} \sin \theta_{\pm} = n_{\pm} \frac{n_1 \sin \theta_1}{n_{\pm}} = n_1 \sin \theta_1 \quad (2.6.1)$$

where  $\theta_2$  is the angle of refraction in the substrate.

The reflections inside the layer can continue until the energy of the light beam depletes. There are thus four kinds of eigenmodes of propagation inside the chiral slab, two in the positive  $z$ -direction (one for each refractive index of the chiral medium) and two on the negative  $z$ -direction, which are given by:

$$E_+^{f,b} = (\pm \cos \theta_+, i, -\sin \theta_+) e^{i(Kx \pm q_+ z)} \quad (2.6.2)$$

$$E_-^{f,b} = (\pm \cos \theta_-, i, -\sin \theta_-) e^{i(Kx \pm q_- z)} \quad (2.6.3)$$

where  $f$  and  $b$  superscripts denote forward and backward propagation inside the slab, and  $+, -$  signs denote the two different refractive indices. To find the total reflection and transmission amplitudes, one should apply the continuity of the electric field with the incident wave, at the  $z=0$  interface, and the transmitted wave, at the  $z=d$  interface.

The incident and reflected waves at the first interface are given by 2.6.2-2.6.3. The total electric field inside the slab is<sup>[6]</sup>:

$$E = f_+ E_+^f + f_- E_-^f + b_+ E_+^b + b_- E_-^b \quad (2.6.4)$$

and the corresponding magnetic field will be

$$H = -i \left( \sqrt{\frac{\epsilon}{\mu}} \right) (f_+ E_+^f - f_- E_-^f + b_+ E_+^b - b_- E_-^b) \quad (2.6.5)$$

A more detailed discussion about the propagation of light inside a chiral slab is made in

paragraph 5.4, along with the description of an optically active etalon, which is the same configuration as the one discussed here, for the case where  $n > n_1 > n_2$ .

## 2.7. Mode and phase matrices

The transmitted fields are given by:

$$E_{2s} = (t_{sp} \cos\theta_2, t_{ss}, -t_{sp} \sin\theta_2) e^{i[Kx + q_2(z-d)]} \quad (2.7.1)$$

$$H_{2s} = \frac{n_2}{\mu_2} (-t_{ss} \cos\theta_2, t_{sp}, t_{ss} \sin\theta_2) e^{i[Kx + q_2(z-d)]} \quad (2.7.2)$$

$$E_{2p} = (t_{pp} \cos\theta_2, t_{ps}, -t_{pp} \sin\theta_2) e^{i[Kx + q_2(z-d)]} \quad (2.7.3)$$

$$H_{2p} = \frac{n_2}{\mu_2} (-t_{ps} \cos\theta_2, t_{pp}, t_{ps} \sin\theta_2) e^{i[Kx + q_2(z-d)]} \quad (2.7.4)$$

Now one has to consider the continuity of the tangential component of  $E_x, E_y, H_x, H_y$  for s and p polarization incident separately. For s polarization, at  $z=0$  we have:

$$r_{sp} c_1 = f_+ c_+ + f_- c_- - b_+ c_+ - b_- c_- \quad (2.7.5)$$

$$1 + r_{ss} = i(f_+ - f_-) + i(b_+ - b_-) \quad (2.7.6)$$

$$-\sqrt{\frac{\epsilon_1}{\mu_1}} r_{sp} = \sqrt{\frac{\epsilon}{\mu}} (f_+ c_+ - f_- c_- - b_+ c_+ + b_- c_-) \quad (2.7.7)$$

$$-\sqrt{\frac{\epsilon_1}{\mu_1}} (1 - r_{ss}) = \sqrt{\frac{\epsilon}{\mu}} (f_+ + f_- + b_+ + b_-) \quad (2.7.8)$$

And at  $z=d$ ,

$$t_{sp} c_2 = f'_+ c_+ + f'_- c_- - b'_+ c_+ - b'_- c_- \quad (2.7.9)$$

$$t_{ss} = i(f'_+ - f'_-) + i(b'_+ - b'_-) \quad (2.7.10)$$



Propagation of light in chiral and achiral materials

$$-\sqrt{\frac{\varepsilon_2}{\mu_2}} t_{ss} c_2 = -i \sqrt{\frac{\varepsilon}{\mu}} (f'_+ c_+ - f'_- c_- - b'_+ c_+ + b'_- c_-) \quad (2.7.11)$$

$$\sqrt{\frac{\varepsilon_1}{\mu_1}} (t_{sp}) = \sqrt{\frac{\varepsilon}{\mu}} (f'_+ + f'_- + b'_+ + b'_-) \quad (2.7.12)$$

with

$$f'_\pm = f_\pm e^{iq_\pm d} \quad (2.7.13)$$

$$b'_\pm = b_\pm e^{-iq_\pm d} \quad (2.7.14)$$

The fields inside the chiral slab for p polarization incident are of the same form, only with different  $f_\pm$  and  $b_\pm$ . Thus both cases can be solved with the same matrices. These matrices were defined by Lekner as a mode matrix  $M$  and a phase matrix  $P$ , which are the following<sup>[6]</sup>:

$$M = \begin{pmatrix} c_+ & c_- & -c_+ & -c_- \\ 1 & 1 & 1 & 1 \\ c_+ & c_- & -c_+ & -c_- \\ 1 & 1 & 1 & 1 \end{pmatrix} \quad P = \begin{pmatrix} e^{iq_+ d} & 0 & 0 & 0 \\ 0 & e^{iq_- d} & 0 & 0 \\ 0 & 0 & e^{-iq_+ d} & 0 \\ 0 & 0 & 0 & e^{-iq_- d} \end{pmatrix} \quad (2.7.15)$$

Lekner also defined the vectors<sup>[6]</sup>:

$$\mathbf{a} = \begin{pmatrix} f_+ \\ f_- \\ b_+ \\ b_- \end{pmatrix} \quad \mathbf{r}_s = \begin{pmatrix} c_1 r_{sp} \\ -i(1+r_{ss}) \\ -i(1-r_{ss})/m \\ -r_{sp}/m \end{pmatrix} \quad \mathbf{r}_p = \begin{pmatrix} c_1(1+r_{pp}) \\ -ir_{ps} \\ ic_1 r_{ps}/m \\ (1-r_{pp})/m \end{pmatrix} \quad (2.7.16)$$

$$\mathbf{t}_s = \begin{pmatrix} c_2 t_{sp} \\ -it_{ss} \\ -ic_2 t_{ss}/m' \\ t_{sp}/m' \end{pmatrix} \quad \mathbf{t}_p = \begin{pmatrix} c_2 t_{pp} \\ -it_{ps} \\ -ic_2 t_{ps} \\ t_{pp}/m \end{pmatrix} \quad (2.7.17)$$

where  $\mathbf{a}$  contains the forward and backward propagation amplitudes, and  $r_s, r_p, t_s, t_p$  vectors contain the total reflection and transmission amplitudes. Since the light beam travels back and forth inside the layer many times, these amplitudes are interpreted as the sum of the proportions of the light energy transmitted from the chiral layer to the substrate (transmission amplitudes) and to the medium of incidence (reflection amplitudes).

We can now express the equations derived at 2.7.5-2.7.12 by the mode and phase matrices. For s polarization incident,

$$\mathbf{r}_s = M \mathbf{a} \quad (2.7.18)$$

$$\mathbf{t}_s = MP \mathbf{a} \quad (2.7.19)$$

The reflection and transmission amplitudes are linked as

$$\mathbf{t}_s = MPM^{-1} \mathbf{r}_s \quad (2.7.20)$$

and as such the matrix L can be defined as

$$L = MPM^{-1} \quad (2.7.21)$$

## **2.8. Evanescent wave and Goos-Hänchen effect**

A discussion about the nature of the evanescent wave should be made, for better understanding of the chiral sensing experiment, which will be presented in section 4. The evanescent wave is a wave which is formed at the interface between two media, when the TIR conditions are satisfied. In order for the boundary conditions at the interface to be satisfied, i.e. the tangential component of the incident and the reflected wave to be continuous, the incident wave is not directly reflected at the exact point where it met the second medium. The solution of the Maxwell equation dictates that, even when  $\theta_1 > \theta_c = \sin^{-1}\left(\frac{n_2}{n_1}\right)$  and as such the light is totally internally reflected, the wave first propagates through the second medium as a traveling wave in the direction along the interface, before passing back to the first medium, and propagate as the reflected wave. The evanescent wave has a penetration depth from some nanometers, at grazing incidence, up to about half a wavelength in the vicinity of the critical angle, and a very short decay time, i.e. time before the wave returns to the first medium. As such, there is a transmitted field, in the form of an evanescent wave which decays exponentially to zero, and so it does not carry energy away from the interface. Thus the

## Propagation of light in chiral and achiral materials

entire process occurs without any intrinsic energy losses, apart from the absorption by the chiral medium, which as the observable quantity of the experiment.

Consider a wave propagating at the  $zx$  direction, through a medium of refractive index  $n_1$ , towards the interface, which lies at the  $z=0$  plane, with a medium of refractive index  $n_2$ . The evanescent wave can be expressed as a transmitted wave using the plane wave equation:

$$E_t = E'' e^{i(k'' \cdot r - \omega t)}$$

Then the continuity at  $z=0$  gives:

$$k'' \cdot r = k'' x \sin \theta_2 - k'' y \cos \theta_2 = k'' x \sin \theta_2 - i k'' z \sqrt{\frac{n_1^2}{n_2^2} \sin^2 \theta_1 - 1}$$

Where we used the Snell's Law and the TIR condition  $\sin \theta_1 > \left(\frac{n_2}{n_1}\right)$  to derive

$$\cos \theta_2 = \sqrt{1 - \sin^2 \theta_2} = \sqrt{1 - \frac{n_1^2}{n_2^2} \sin^2 \theta_1} = i \sqrt{\frac{n_1^2}{n_2^2} \sin^2 \theta_1 - 1}$$

So the transmission wave equation becomes

$$E_t = E'' e^{-\alpha |z|} e^{i(k_1'' x - \omega t)}$$

where

$$\alpha = k'' \sqrt{\frac{n_1^2}{n_2^2} \sin^2 \theta_1 - 1} \quad \text{and} \quad k_1 = k'' \sin \theta_1 \frac{n_2}{n_1}$$

The form of the transmission wave equation obtained gives the picture of the evanescent wave. The first term,  $e^{-\alpha |z|}$  shows that the wave amplitude drops off exponentially as it propagates away from the interface, into the optically sparser medium. The second term shows that the evanescent wave can be described in terms of many constant phase wave surfaces moving parallel to the interface with a speed  $\frac{\omega}{k_1}$ .

Thus the mathematical approach of the evanescent wave confirms the picture described earlier, that of a travelling wave with a small penetration depth, that exponentially decays upon its transmission to the other side of the interface.

The complex value of  $\theta_2$ , which is produced at TIR conditions, leads to a complex value of the respective Fresnel coefficients for angles beyond the critical angle of incidence. The coefficients become, for TIR,

Propagation of light in chiral and achiral materials

$$r_s = -\frac{\cos\theta_1 - i\sqrt{\sin^2\theta_1 - n^2}}{\cos\theta_1 + i\sqrt{\sin^2\theta_1 - n^2}} \quad (2.8.1)$$

$$r_p = -\frac{n^2 \cos\theta_1 + i\sqrt{\sin^2\theta_1 - n^2}}{n^2 \cos\theta_1 + i\sqrt{\sin^2\theta_1 - n^2}} \quad (2.8.2)$$

The squares of the absolute values of  $r_s$ ,  $r_p$  are equal to 1, so the light is totally internally reflected, but the actual values are not real. This implies a change in the phase of the coefficients, and that, since the imaginary part contains the angle of incidence, this change of phase is a function of the angle. To calculate this change, we first state that since  $|r_s|^2 = |r_p|^2 = 1$ , we can express the coefficients and their respective numerators and denominators as *amplitude*· $e^{-i\text{phase}}$ :

$$r_s = 1 \cdot e^{-i\delta_s} = \frac{ae^{-i\alpha}}{ae^{+i\alpha}} \quad (2.8.3)$$

$$r_p = -1 \cdot e^{-i\delta_p} = -\frac{\beta e^{-i\beta}}{\beta e^{+i\beta}} \quad (2.8.4)$$

which give us  $\delta_s = 2\alpha$  and  $\delta_p = 2\beta$ . By comparing each numerator and denominator of eqs 2.8.3-2.8.4 with the corresponding terms in eqs 2.8.1-2.8.2, we obtain

$$a e^{i\alpha} = \cos\theta_1 + i\sqrt{\sin^2\theta_1 - \left(\frac{n_2}{n_1}\right)^2} \quad (2.8.5)$$

$$b e^{i\beta} = \left(\frac{n_2}{n_1}\right)^2 \cos\theta_1 + i\sqrt{\sin^2\theta_1 - \left(\frac{n_2}{n_1}\right)^2} \quad (2.8.6)$$

Another way of expressing the process of the TIR at an interface is by the Goos-Hänchen effect. This effect was discovered experimentally in 1949 by Hermann Fritz Gustav Goos and Hilda Hänchen, and describes how a linearly polarized light wave undergoes a small lateral shift when totally internally reflected. This comes in conflict with the geometric optics picture of TIR, where the wave is reflected at the exact same point of space where it reached the interface, and which was adopted as the description of reflection by classical optics before the discovery of Goos-Hänchen shift.

## Propagation of light in chiral and achiral materials

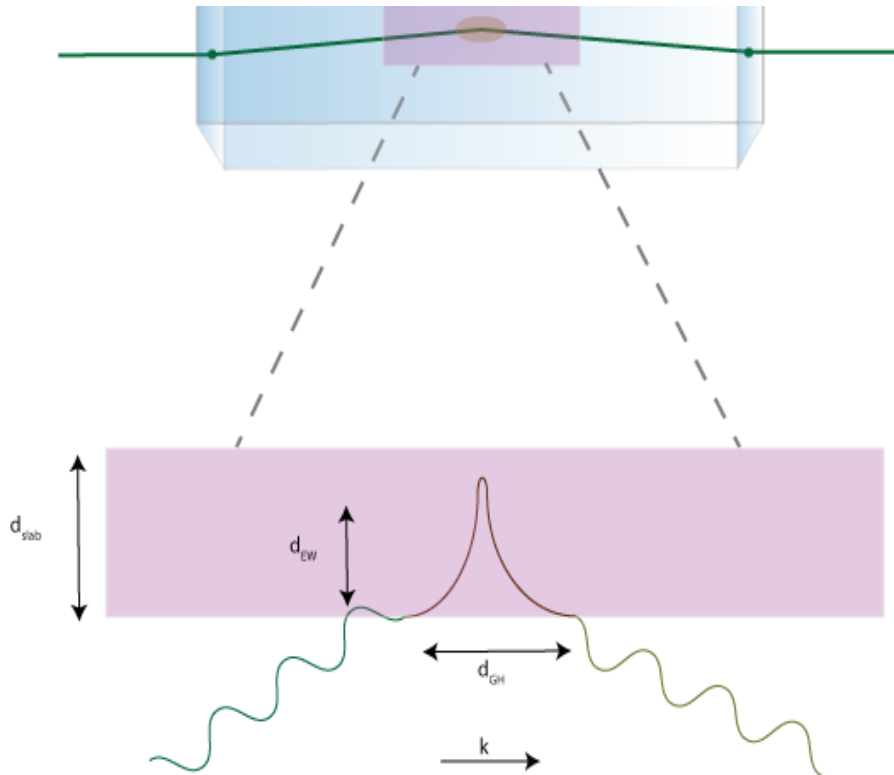


Figure 10: a) View from above of the light wave travel through a chiral medium in terms of geometrical optics. The wave propagates through the prism and is totally internally reflected after incidence with the prism-chiral medium interface. The TIR gives rise to an evanescent wave at the vicinity of the reflection b) View from side of the prism-chiral medium interface. The light wave incident to the interface forms an evanescent wave, emerging at the point where it meets the interface. The wave formed is a standing wave, which decays exponentially, and undergoes a lateral displacement, which is the Goos-Hänchen shift.

An explanation of the Goos-Hänchen lateral shift starts by considering a wave incident at an interface as a superposition of infinitely extended plane waves. Since this wave has spatial dimensions, there is a certain spatial distribution of the beam energy, and not all plane waves have the same angle of incidence. But, each plane wave undergoes a different phase shift upon the reflection at the interface, which is dependent on its angle of incidence. The cumulative phase shift of all these plane waves leads to a change to the transverse shape of the beam, since this depends on the amplitude and the phase of the superimposition of the plane waves. This way, a transverse displacement in the beam occurs upon the interface. This displacement is very small at normal incidence, and becomes larger with a larger angle of incidence. At the critical angle, the Goos-Hänchen shift is infinite, as described by the classical picture of reflection.

A picture of the Goos-Hänchen shift, in terms of wave propagation, is given in figure

10b. The lateral shift at the beam path is shown, as is the evanescent wave formed beyond the interface. The lateral shift can be interpreted as the length of propagation of the evanescent wave parallel to the interface, and for this it is used as a more precise interpretation for the probing of the beam at the second medium. The evanescent wave interpretation is not sufficient for explaining the ability to measure a chiral signal; since the wave propagates back and forth in the  $z$  direction, the perpendicular to the interface, the optical rotation induced while propagating forward will cancel out with the one induced at backward propagation. Thus the physical quantity needed to explain chiral optical rotation is the goos-Hänchen length.

Consider a wave of both s and p polarization components. Each component will undergo a different phase shift, namely<sup>[9]</sup>

$$\varphi_{Rs} = -2 \tan^{-1} \left( \frac{\sqrt{\sin^2 \theta_i - n^2}}{\cos \theta_i} \right) \quad (2.8.7)$$

$$\varphi_{Rp} = -2 \tan^{-1} \left( \frac{\sqrt{\sin^2 \theta_i - n^2}}{n^2 \cos \theta_i} \right) \quad (2.8.8)$$

the lateral displacement  $s$  will be

$$s = - \frac{\partial \varphi}{\partial k_{1y}} \quad (2.8.9)$$

where  $k_{1y}$  is the parallel component of the wavevector, so

$$s = - \frac{\partial \varphi}{\partial k_{1y}} = - \frac{1}{k_1 \cos \theta_i} \frac{d\varphi}{d\theta} \quad (2.8.10)$$

and the GHS for each polarization will be the corresponding component of the lateral displacement

$$D_s = s_s \cos \theta_i = \frac{\lambda_1}{\pi} \frac{\sin \theta_i}{\sqrt{\sin^2 \theta_i - n^2}} \quad (2.8.11)$$

$$D_p = s_p \sin \theta_i = \frac{n^2}{\sin^2 \theta_i (1 + n^2) - n^2} D_s \quad (2.8.12)$$

This result confirms the existence of an ellipsometric phase shift upon the reflection of an interface. The two polarization components undergo different lateral shift, and as a result a phase shift is acquired by the reflected beam.

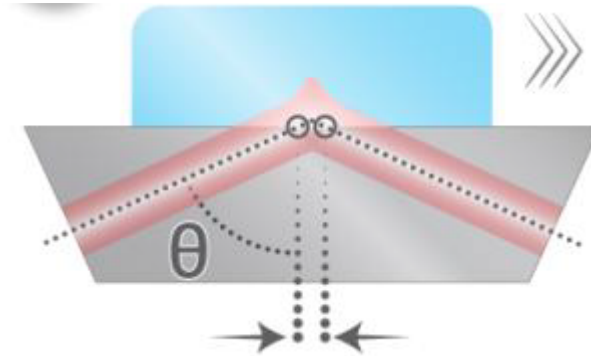


*Figure 11: Forming of the evanescent wave at the prism-sample interface*

## 3. Optical Cavity Ring-Down Techniques

### 3.1. Introduction

Optical cavities are used for the enhancement of absorption signal measurements, as a means to improve the sensitivity and time resolution. It was O'Keefe and Deacon<sup>[10]</sup> who first used an optical cavity for absorption spectroscopy measurements using a pulsed laser, introducing Cavity Ring-Down Spectroscopy (CRDS). Since then, numerous measurements in gaseous and liquid samples were made using cavity-enhanced methods.

The great advantage of cavity-enhanced experiments is that they are table-top configurations, which can multiply the optical path by orders of magnitude. This results in many passes of the laser beam, which is used to probe the absorbing medium, and as such an absorption signal enhanced by as many times as are the passes through the medium. For weak signals to be measurable, a high-finesse cavity is needed. High-

## Optical Cavity Ring-Down Techniques

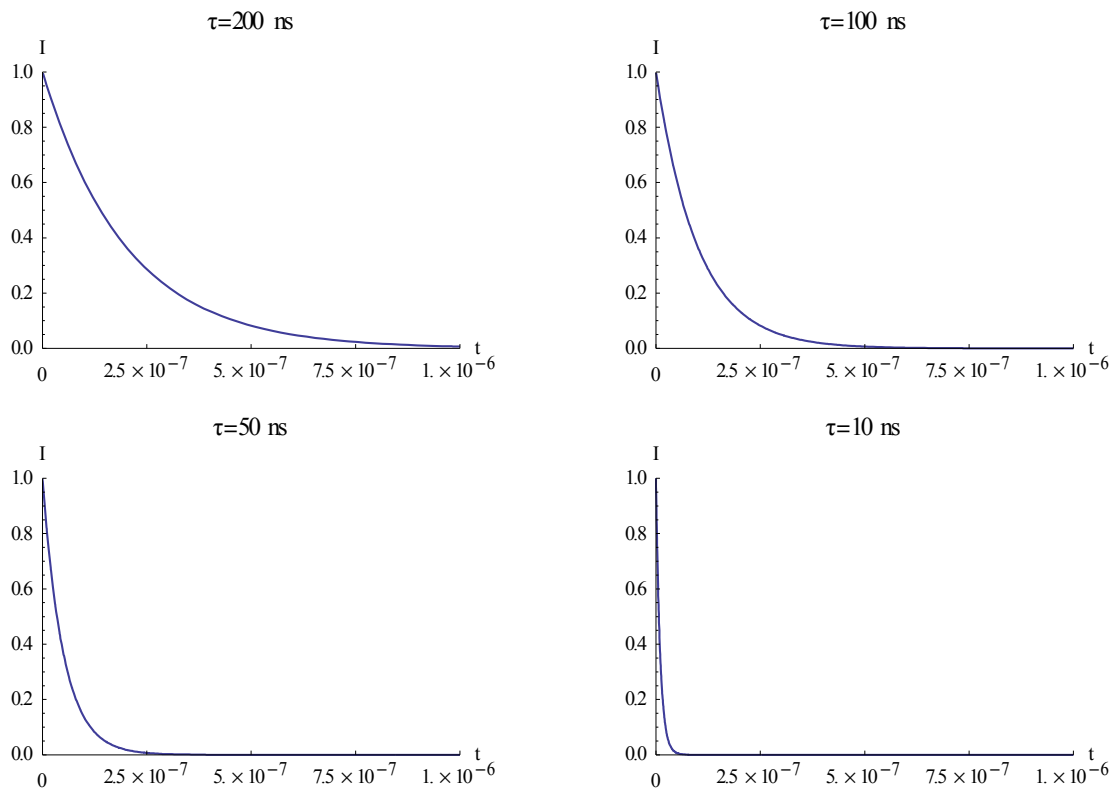


Figure 12: CRDS traces for various gases with different decay times

finesse cavities are constructed using mirrors with high reflectance ( $>0.99$ ), which keep more energy inside the cavity after every reflection, thus allowing more passes back and forth into the cavity before the pulse energy escapes.

In this section, we describe the various techniques which use Cavity Ring-Down methods, giving basic theory and examples of data for each one. Cavity Ring-Down Spectroscopy (CRDS) is mentioned first, followed by Cavity Ring-Down Ellipsometry (CRDE). Then EW-CRDE is analyzed, an ellipsometric technique where the evanescent wave is used as a probe of the liquid sample. The theory of this configuration is discussed in more depth, as it explains a big portion of the theory related to the experiments which will be presented later in this thesis. Finally, a novel method for measuring chiral samples is presented, based on EW-CRDS, able to measure weak chiral signals in environments with high noise, with the use of signal reversals.

### 3.2. Cavity Ring-Down Spectroscopy (CRDS)

CRDS is a highly sensitive absorption spectroscopy technique, used to measure



## Optical Cavity Ring-Down Techniques

optical extinction of light-absorbing samples. In this technique, a laser pulse is trapped inside a resonant cavity consisting of two highly reflecting mirrors<sup>[10]</sup>, as in fig.1. Because a mirror cannot reflect 100% of the light incident to it, the pulse energy will decrease during each round-trip into the cavity by a fixed percentage, owing to these reflectivity losses and scattering. The intensity of the energy will then be

$$I = I_0 e^{-t/\tau} \quad (3.2.1)$$

where  $I_0$  is the initial intensity and  $\tau$  is the decay constant or ring-down time. The decay time is defined as the time taken for the intensity to fall to  $1/e$  of the initial value. Depending on how much light is absorbed by any sample introduced inside the cavity, this ring-down time will be different. A strongly absorbing medium would give a smaller  $\tau$ , because the light intensity will be drained much faster. Figures 12(a-d) show different ring-down traces for different ring-down times.

The measurable quantity of CRDS is the decadic absorbance. This is a factor of how much light energy can the gas in the cavity absorb. It is measured through the observation of the difference in the decay time of the trace. The decay time of the laser beam in an empty cavity is given by

$$\tau_0 = \frac{n}{c} \frac{l}{1-R+X} \quad (3.2.2)$$

Where  $n$  is the index of refraction,  $c$  is the speed of light,  $l$  is the cavity length,  $R$  is the mirror reflectivity, and  $X$  describes other miscellaneous optical losses.

Assuming now a cavity filled with the gaseous sample, the decay time is

$$\tau_0 = \frac{n}{c} \frac{l}{1-R+X+al} \quad (3.2.3)$$

Where  $a$  is the absorption coefficient of the sample. The decadic absorbance will then be given by

$$A = \frac{n}{c} \frac{l}{2.303} \left( \frac{1}{\tau} - \frac{1}{\tau_0} \right) \quad (3.2.4)$$

### 3.3. Cavity Ring-Down Ellipsometry (CRDE)

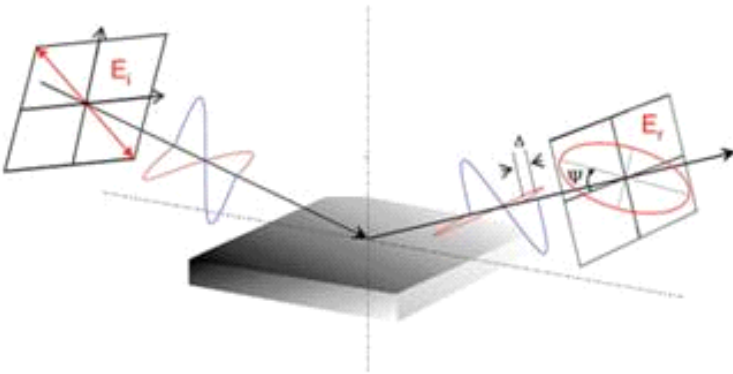


Figure 13: Simple ellipsometric configuration

Ellipsometry is a well-established technique for probing the dielectric properties of thin films. It is used for the measurement of quantities such as the thickness, composition and doping concentration of the measured surface among others. Ellipsometry can generally measure any physical property of a material that alters in any way the polarization of light. For this reason, it is a very versatile technique used in many fields, from semiconductor physics and optics, to pharmacology and biology.

The measurables in ellipsometry are two independent quantities:  $\Psi$ , the amplitude ratio between the two polarization components,  $r_s$  and  $r_p$ , and  $\Delta$ , the phase difference between these two components, connected by the formula

$$\frac{r_p}{r_s} = \tan(\Psi) e^{i\Delta} \quad (3.3.1)$$

Although ellipsometry is a technique that has evolved through its many years of existence, research for improving it in terms of speed and sensitivity is continuing. Current state-of-the-art ellipsometers require data acquisition times in the order of milliseconds, which can be even higher when ultra-high resolution is required.

Karaiskou et al.<sup>[11]</sup> used a CRD configuration to make fast and sensitive ellipsometric measurements. They were able to simultaneously measure the ellipsometric parameters  $\Psi$  and  $\Delta$  of a gaseous fenchone sample adsorbing to high-reflectivity mirrors of a cavity, with a phase sensitivity of  $10^{-2}$  degrees and a time sensitivity of  $1 \mu\text{s}$ . They achieved that by using a pulsed laser of 30 ns pulse width and 10 Hz pulse repetition rate to probe the sample, tracking the time evolution of the pulse (see fig. 15a). When the pulse passed through the sample, a phase shift was introduced in the s and p vectors of the polarization leading to an alteration to the overall polarization, from linear to elliptical and back. This change was tracked using a balanced polarimeter configuration at the exit, and the result was an exponential decay with an oscillation imprinted on it (see fig. 15b). This oscillation was identified as the trademark of the phase shift, so

## Optical Cavity Ring-Down Techniques

measuring its frequency, the phase shift value could be extracted.

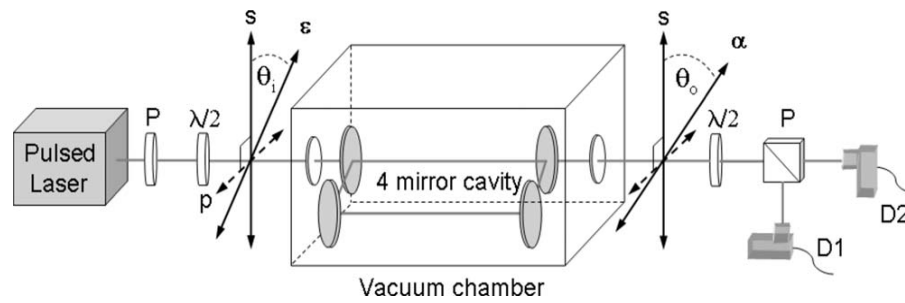


Figure 14: CRDE configuration <sup>[11]</sup>

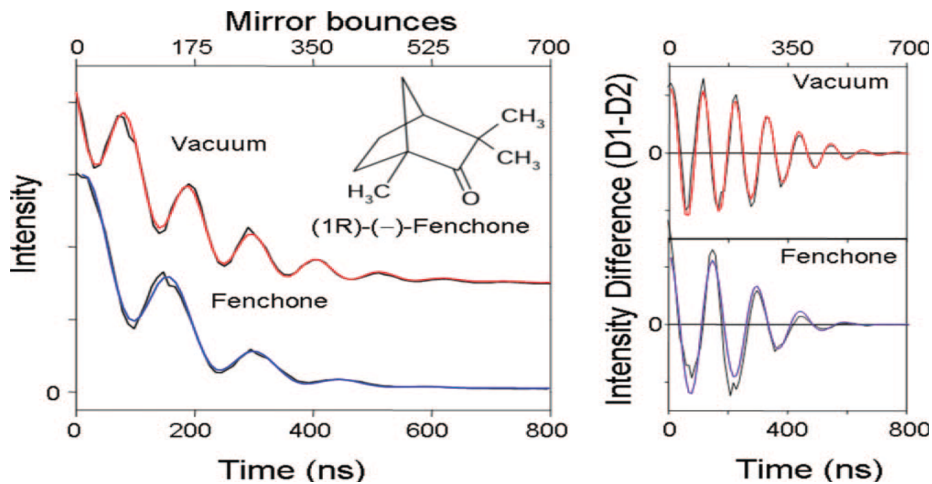


Figure 15: Raw (black) and fitted (colored) CRDE data for Fenchone. Note the change in the oscillation frequency between the vacuum and the fenchone traces. This frequency difference is proportional to the phase shift that fenchone introduces in the light polarizations.

The time resolution was only limited by the laser repetition rate and the detection electronics used.

### 3.4. Evanescent wave Cavity Ring-Down Ellipsometry (EW-CRDE)

The technique was modified by Everest et al.<sup>[12]</sup> to be used for the measurement of liquid samples, with the use of the evanescent wave which is formed beyond the interface between two media with different refractive indices, when the wave is totally internally reflected. When an optical probe (e.g. a light beam) is incident to a liquid-solid or gas-solid interface, at an angle bigger than the critical angle of incidence [ $\theta_c = \arcsin(n_1/n_s)$ ], and thus TIR conditions are in effect, an evanescent wave is formed

at the liquid side of the interface(see figure 11). Propagation through the liquid, as in gas CRDE, introduces a phase shift between the s and p polarization of incidence. A prism is introduced into the cavity to serve as the medium of incidence in the liquid-solid interface. If the TIR conditions are matched, the pulse exits from the opposite side of the prism, and continues travelling back and forth inside the cavity, until its energy fades out. The phase shift of each pass is again added to the total, so the measured phase shift is enhanced by the number of passes ( $\sim 100$  for mirror reflectivities of 0.99).  
 TI

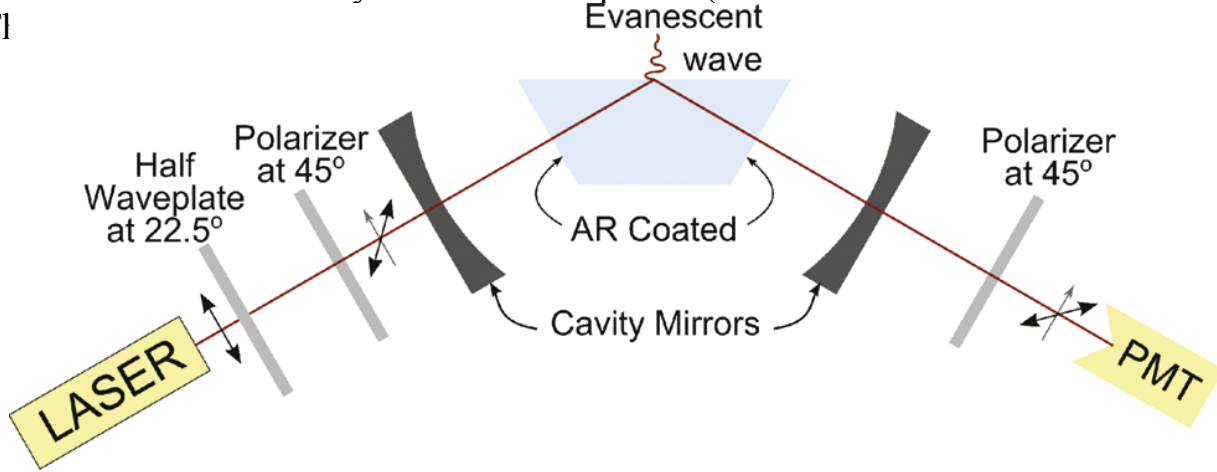


Figure 16: EW-CRDE experimental configuration

Theoretical analysis of EW-CRDE was done by Stamataki et al.<sup>[13]</sup>. Consider a laser pulse entering into a cavity of length  $d$ , made by two mirrors of reflectivity  $R_m \approx 0.99$  put opposite to one another. As we saw earlier, the pulse time evolution will be given by  $I = I_0 e^{-t/\tau}$ . The decay time  $\tau$  is given by

$$\tau = \frac{d/c}{1 - R_m} \tag{3.4.1}$$

In general, the mirrors have different reflectivities for s and p polarizations. For that reason, we shall derive the time evolution of the pulse in an ellipsometric configuration, by treating separately the electric field amplitudes of each polarization, then take  $|E_s(t) + E_p(t)|^2$ .

The laser pulse makes  $N$  round-trips inside the cavity. The electric field that passes through the detector outside of the cavity, will then be  $E_s(0)E_s(N)$ , where  $E_s(0)$  is the amplitude of the electric field that passes through the mirror without making any round-trips ( $\sim 0.01\%$  of the initial pulse energy), and  $E_s(N)$  is the respective amplitude for  $N$  round-trips.

For the directly passing component,

## Optical Cavity Ring-Down Techniques

$$E_s(0) = E^0(1 - R_m)(\sqrt{R_s}) \cos \theta_i \cos \theta_o e^{i\phi_s} \quad (3.4.2)$$

And for  $E_s(N)$

$$E_s(N) = E_s^0(\sqrt{R_m})^{2N}(\sqrt{R_s})^{2N} e^{2iN\phi_s} \quad (3.4.3)$$

Eq. (4) can be simplified, by expressing the number of round-trips  $N$  in terms of time elapsed,  $N = \frac{ct}{2d}$ . The terms  $(R_m R_s)^N$  can also be approximated by  $e^{-t/(2\tau_s)}$ . By substituting these two expressions in (3), we get

$$E_s(t) = E_s^0 e^{-t/(2\tau_s)} e^{ict\phi_s/d} \quad (3.4.4)$$

with

$$\tau_s = \frac{d/c}{1 - R_m R_s} \quad (3.4.5)$$

The respective expressions for the p-polarization will be

$$E_p(N) = E_p^0(\sqrt{R_m})^{2N}(\sqrt{R_p})^{2N} e^{2iN\phi_p} \quad (3.4.6)$$

$$E_p(0) = E^0(1 - R_m)(\sqrt{R_p}) \cos \theta_i \cos \theta_o e^{i\phi_p} \quad (3.4.7)$$

$$E_p(t) = E_p^0 e^{-t/(2\tau_p)} e^{ict\phi_p/d} \quad (3.4.8)$$

$$\tau_p = \frac{d/c}{1 - R_m R_p} \quad (3.4.9)$$

The full expression of the light intensity will then be obtained by finding the squared sum of the amplitudes of the two polarization components, i.e.  $|E_s(t) + E_p(t)|^2$ :

$$I(t) = |E_s(t) + E_p(t)|^2 = I_o(1 - R_m)^2 (R_s \cos^2 \theta_i \cos^2 \theta_o e^{-t/\tau_s} + R_p \sin^2 \theta_i \sin^2 \theta_o e^{-t/\tau_p}) + (2\sqrt{R_s R_p} \sin \theta_i \cos \theta_i \sin \theta_o \cos \theta_o e^{-(1/\tau_s + 1/\tau_p)t/2} \cos(\omega t + \Delta)) \quad (3.4.10)$$

where

$$\omega = c\Delta/d \quad (3.4.11)$$

## Optical Cavity Ring-Down Techniques

and  $\Delta$  is the phase difference between the two polarizations,  $\phi_p - \phi_s$ . By approximating  $R_s \sim R_p \sim 1$ , which is the case for the TIR surface reflection i.e. the prism/liquid interface, and setting  $\theta_i = \theta_o = 45^\circ$ , eq(3.4.10) becomes

$$I = AI_o e^{-t/\tau} \cos^2\left(\frac{\omega t + \Delta}{2}\right) \quad (3.4.12)$$

where A is a normalization constant. For use at an experimental fit, the more convenient expression

$$I = I_o e^{-t/\tau} \cos^2(\omega t/2 + \phi) + B \quad (3.4.13)$$

is used, where  $\phi$  is the phase of the polarization beating with respect to the phase of the laser pulse (ideally  $\Delta/2$ ) and B is a constant added to compensate for experimental imperfections due to low modulation depth of the beating. Note that the constant B is not a product of the calculation, but an experimental constant introduced for a more realistic fit of the data. In ideal experimental conditions, this constant would be equal to 0.

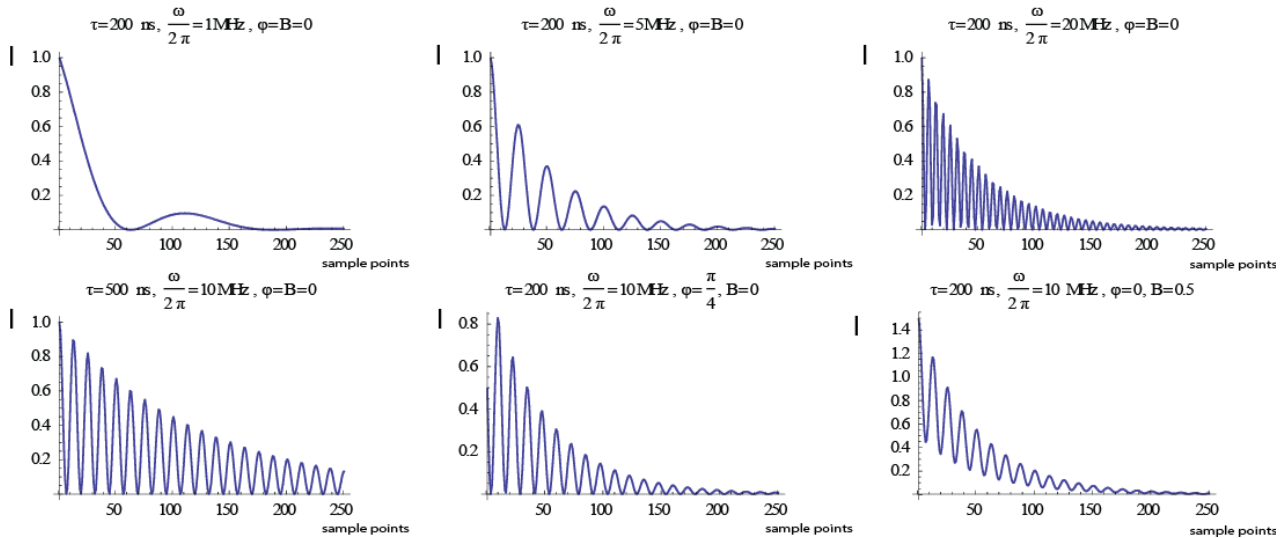


Figure 17: EW-CRDE traces for various values of  $\tau$ ,  $\omega$ ,  $\phi$  and B

These traces show how the measured signal from the detector varies with  $\tau$ ,  $\omega$ ,  $\phi$  and B. When the beating frequency is very low, the data resemble to those of a CRDS measurement. The beating is not easily distinguished, and there seems to be only an exponential decay in the data. In this case, the polarization changes very slowly, slower than the time window used (here 1  $\mu$ s), and so it is not detected in the trace. The next

two traces are for experimental data with the same ring-down time (200 ns) but different beating frequencies (5 and 20 MHz respectively). One can see that the decay envelope fades out at the same point of time, but with more oscillations for higher frequency. In the next figure, there is a trace with 500 ns ring-down time, which fades out completely in more than 1  $\mu$ s. The fifth trace is displaced by  $\varphi=\pi/4$  with respect to the one above of it, which is at the same conditions other than the phase difference. In the last plot, one can see the effect of  $B$ , a small raise in the modulation depth of the first.

### 3.5. Chiral CRD

The nature of chirality dictates an alteration in the application of the technique used in EW-CRDE, which consists of a linear cavity with one beam propagating forward and backwards. Unlike optical rotation induced by non-chiral materials, chiral optical rotation is canceled out when the beam propagates in a round-trip. The symmetry of the effect is opposite than the symmetry of non-chiral(Faraday) optical rotation. This means that, once a beam passes through a chiral sample, thus rotating its plane of polarization at a certain direction, passing backwards from the same spot would induce the opposite optical rotation, which results in total optical rotation equal to zero. This way, chirality effects cannot be measured in a plain linear cavity.

A way of evading the cancellation of the chirality signal even in linear cavities was proposed by Evtuhov and Siegman<sup>[14]</sup> and Kastler<sup>[15]</sup>. They proposed introducing two intracavity quarter waveplates in zero angle, one in each side of the cavity. Vaccaro et al.<sup>[16][17]</sup> then proposed a way to suppress the spurious linear birefringence. They offset the optical axes of the quarter waveplates by an angle  $\alpha(\sim 5^\circ)$ , thus introducing a circular birefringence of  $2\alpha$  per round-trip of light inside the cavity.

Although the configuration described above could give a solution to the first two problems, the weakness of the chiral signal and the spurious linear birefringences, there remains a last limitation in the process. The required removal of the sample, or else the inability of the configuration to produce absolute chirality measurements, without the use of an offset sample.

To surpass this limitation, Bougas et al.<sup>[1]</sup> proposed a bowtie ring cavity. The main advantage of such a cavity is that it can support two counter-propagating laser beams which could be used as one more signal reversal, by subtracting the measurements of one by the other. To break the symmetry between the two counter-propagating beams, a magneto-optical window is used, in the effect of a longitudinal magnetic field  $\mathbf{B}$ , which induces a Faraday rotation  $\theta_F$ . Because the chiral effect  $\varphi_c$  and the Faraday rotation have different symmetries (see fig 1) the optical rotations measured for each beam can be distinguished. Considering the laboratory frame,  $\theta_F$  has the same sign for both beams,

## Optical Cavity Ring-Down Techniques

since it is only determined by  $\mathbf{B}$ , while  $\varphi_c$  is determined by the propagation direction, and has different signal for each beam. Therefore, the measured single-pass optical rotation of each beam is:

$$\theta_{CW} = \theta_F + \varphi_c \quad (3.5.1)$$

$$\theta_{CCW} = \theta_F - \varphi_c \quad (3.5.2)$$

Traversing through the cavity, the light polarization rotates with angular frequencies

$$\omega_{CW}(\pm B) = (\pm\theta_F + \varphi_c) c / L \quad (3.5.3)$$

$$\omega_{CCW}(\pm B) = (\pm\theta_F - \varphi_c) c / L \quad (3.5.4)$$

$L$  being the round-trip cavity length. Taking the difference of the frequencies of the two beams, we have

$$\Delta\omega(\pm B) = |\omega_{CW}(\pm B)| - |\omega_{CCW}(\pm B)| = \pm 2\varphi_c (c/L) \quad (3.5.5)$$

Thus inverting the  $B$  sign, we can invert the chirality sign. Doing so, we obtain the final result

$$\Delta\omega(B) - \Delta\omega(-B) = 4\varphi_c (c/L) \quad (3.5.6)$$

The chiral signal becomes 4 times larger for two signal reversals, since it is odd under both direction and magnetic field reversal. The background, on the other hand, cancels.

*Figure 18: Chiral CRD experimental setup.*



### 3.6. Other types of running cavities

At this point, we have to make a discussion about why a bowtie cavity was used, instead of any other kind of running cavity, such as a triangular or orthogonal cavity.

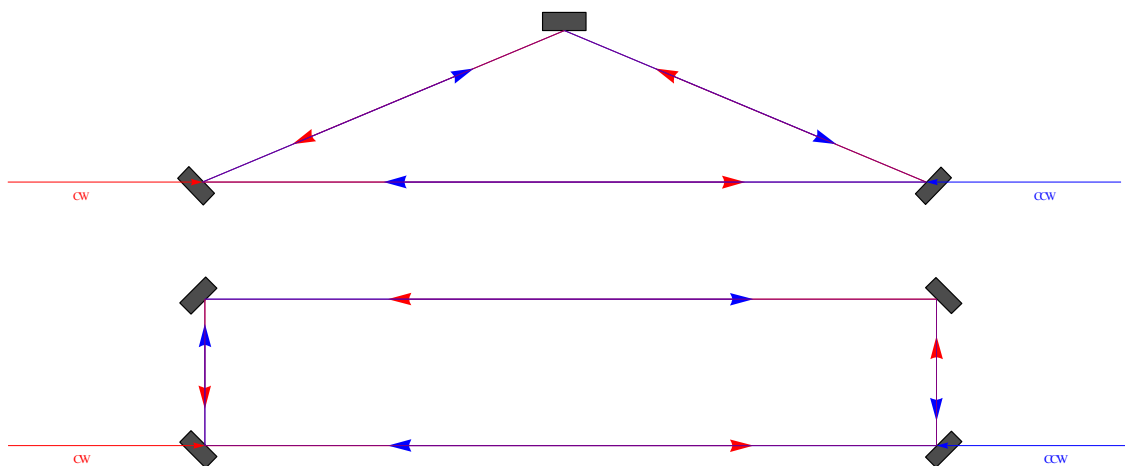


Figure 19: Possible configurations for running cavities with counter-propagating beams

This is because either of these configurations introduce a large angle of reflection at the mirror, which in turn introduces an ellipsometric phase shift in the s-p components of the beam field. In order for this shift to be totally suppressed, it should be much smaller than the Faraday rotation introduced in the cavity ( $\Delta_f \gg \delta_\epsilon$ ). This is managed by setting the reflection angle to as much smaller as it can, because the amplitude of the phase shift is directly proportional to the reflection angle. A bowtie cavity with a small distance between the two adjacent mirrors M2 and M3 (see figure 20) has a small reflection angle for all four mirrors, so the phase shift introduced is lower than with any other configuration.

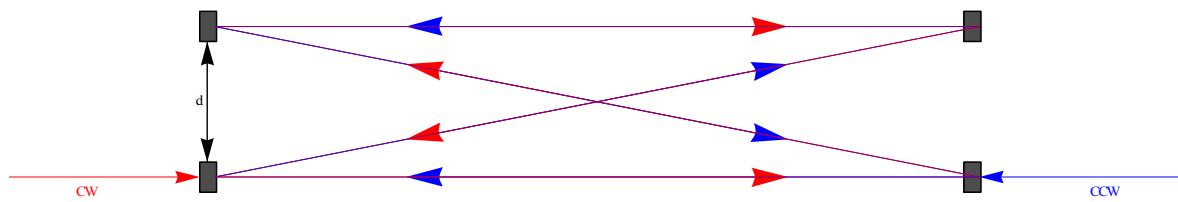


Figure 20: Running bowtie cavity

## 4. Evanescent-wave chiral sensing via signal reversing cavity-enhanced polarimetry

### 4.1. Introduction

The discussions made earlier about the forming of an evanescent wave in TIR conditions, the induced optical rotation and the way this rotation can be measured for a chiral medium using a CRD technique were applied in Sofikitis et al.<sup>[2]</sup>. Here we present the results of the evanescent-wave chiral sensing.

#### 4.1.1. Experimental setup

As noted before, a bow-tie ring-down cavity is used for enhancing the chiral signal. An anti-reflection coated Dove prism is inserted on one arm of the cavity, which serves as the medium of incidence of the chiral slab configuration that was examined earlier. The liquid chiral sample to be measured is deposited on the prism, forming a thick (compared to the laser wavelength) layer upon it. A laser pulse of 800 nm wavelength and 35 fs pulse width is inserted in the cavity into both CW and CCW directions. The Dove prism has a sharp angle of 70 degrees (figure 21), which leads to a 84 degree angle of incidence at the prism-layer interface, when light enters the prism horizontally. Its dimensions are 80x25x25 mm.

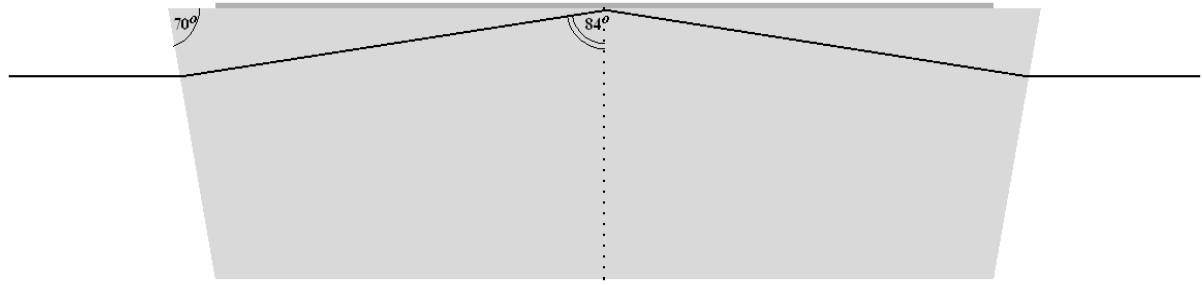


Figure 21: Light propagation inside the prism

TIR conditions are maintained through all passes from the cavity. The time-dependent intensity of the output light decays exponentially as  $e^{-t/\tau_0}$ , where the photon lifetime is

$$\tau_0 = L/[c(1 - R^4)] \approx 1 \mu s \quad (4.1.1)$$

. A 0.3 T magnetic field is applied to a 3 mm thick terbium gallium garnet (TGG) crystal, to introduce a Faraday rotation  $\theta_F = 2.5-4^\circ$ , which breaks the phase shift symmetry between CW and CCW beam, as noted earlier.

A polarizer is used at the output, which alters the pulse signal, inserting oscillations with frequency  $\omega_{CW}, \omega_{CCW}$  at the CW and CCW beams respectively:

$$I_{CW} = I_o e^{-t/\tau_0} \cos^2[\omega_{CW} t/2] \quad (4.1.2)$$

$$I_{CCW} = I_o e^{-t/\tau_0} \cos^2[\omega_{CCW} t/2] \quad (4.1.3)$$

where  $I_o$  is the output intensity at  $t=0$ .

All intracavity optics are anti-reflection coated for 800 nm.

The samples measured here are solutions of maltodextrin ( $\gamma = 4.2 \cdot 10^{-6} c_M$ ) and fructose ( $\gamma = -2.28 \cdot 10^{-6} c_M$ ).  $c_F$  and  $c_M$  are the respective concentrations of chiral material in its solution with water, and it should be known to define its chirality factor.

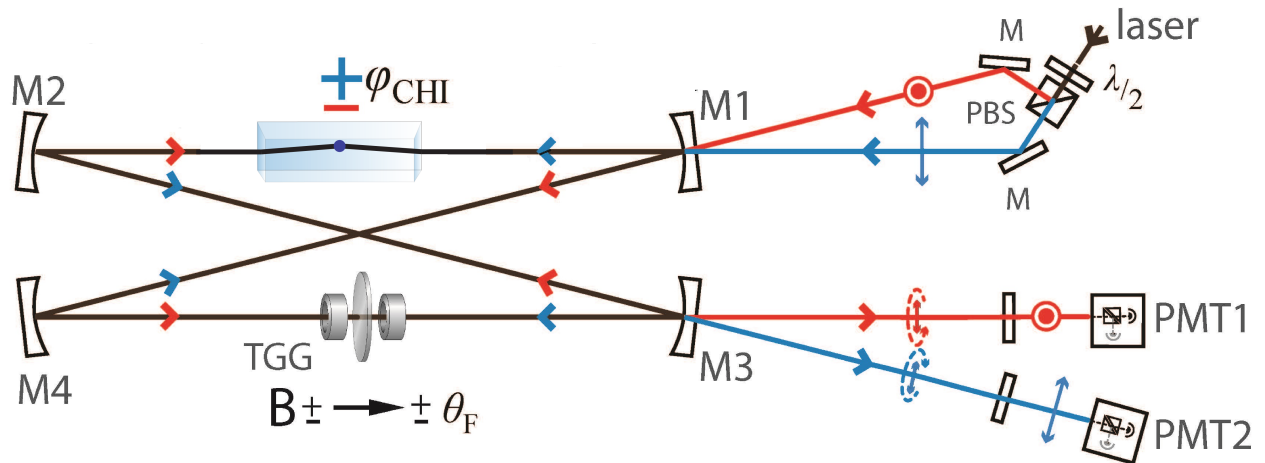


Figure 22: Experimental setup of chiral CRD measurements

#### 4.1.2. Derivation of the optical rotation measurement formula

The experimental values which are obtained with the method previously analysed are to be compared with a theoretical formula derived from Silverman<sup>[5]</sup>

$$\varphi_{EW} = \frac{\Delta n}{n} \frac{N^2}{1-N^2} \frac{\cos\theta_1}{\sqrt{\sin^2\theta_1 - N^2}} \quad (4.1.4)$$

Here we show how the theory of the chiral layer, which we discussed earlier, gives this formula.

The solution that is injected into the flow cell forms a layer of thickness  $\sim 200 \mu\text{m}$  upon the prism, and of some centimeters of width. These dimensions are considered much larger than the wavelength of light. Thus, we can consider the layer formed not as a chiral slab, but as an infinite chiral medium over the prism. Doing so, and considering TIR conditions, the reflection amplitudes  $r_{++}$  and  $r_{--}$  are given by<sup>[6]</sup>:

$$r_{++} = (c_1 - c_+)(c_1 + c_-) / D \quad (4.1.5)$$

$$r_{--} = (c_1 + c_+)(c_1 - c_-) / D \quad (4.1.6)$$

The observable here is the optical rotation that is introduced at the evanescent wave from the chiral layer. This is given by

$$\varphi_{EW} = \text{Arg} \left[ \frac{1}{2} \frac{r_{++}}{r_{--}} \right] = \text{Arg} \left[ \frac{\left( \cos\theta_1 - \sqrt{1 - \left( \frac{n \sin\theta_1}{n + dn/2} \right)^2} \right) \left( \cos\theta_1 + \sqrt{1 - \left( \frac{n \sin\theta_1}{n - dn/2} \right)^2} \right)}{\left( \cos\theta_1 + \sqrt{1 - \left( \frac{n \sin\theta_1}{n - dn/2} \right)^2} \right) \left( \cos\theta_1 - \sqrt{1 - \left( \frac{n \sin\theta_1}{n + dn/2} \right)^2} \right)} \right] \quad (4.1.7)$$

where  $dn=2\gamma$ , the difference between the two refractive indices of the chiral material. The factor  $\frac{1}{2}$  is there because the argument of  $\frac{r_{++}}{r_{--}}$  gives double the actual phase shift.

Expanding the argument around  $dn=0$  we get

$$\begin{aligned} \frac{r_{++}}{r_{--}} &= 1 + \frac{2\cos\theta_1 n_1^2 \sin^2\theta_1 \Delta n}{n^3 \sqrt{\frac{n^2 - n_1^2 \sin^2\theta_1}{n^2}} \left( -\cos\theta_1 + \sqrt{\frac{n^2 - n_1^2 \sin^2\theta_1}{n^2}} \right) \left( \cos\theta_1 + \sqrt{\frac{n^2 - n_1^2 \sin^2\theta_1}{n - dn/2}} \right)} \\ &= 1 + \frac{2\cos\theta_1 n_1^2 \sin^2\theta_1 \Delta n}{n^3 \sqrt{1 - \frac{n_1^2 \sin^2\theta_1}{n^2}} \left( 1 - \frac{n_1^2}{n^2} \right) \sin^2\theta_1} \end{aligned} \quad (4.1.8)$$

we name  $N = \frac{n}{n_1}$  and take into consideration that, under TIR conditions,  $\frac{n_1^2 \sin^2\theta_1}{n^2} > 1$ , which makes the argument of the square root negative. From there we proceed as:

$$\begin{aligned} \frac{r_{++}}{r_{--}} &= 1 - i \frac{2\cos\theta_1 n_1^2 \sin^2\theta_1 \Delta n}{n^3 \left( 1 - \frac{1}{N^2} \right) \sin^2\theta_1 \sqrt{\frac{\sin^2\theta_1}{N^2} - 1}} = 1 - i \frac{2\cos\theta_1 n_1^2 \Delta n}{n N^2 (1 - N^2) \frac{1}{N^2} \frac{1}{N} \sqrt{\sin^2\theta_1 - N^2}} \\ &= 1 - i \frac{2 N \cos\theta_1 \Delta n}{n \sqrt{\sin^2\theta_1 - N^2} (1 - N^2)} = 1 - 2i \frac{\Delta n}{n} \frac{N}{(1 - N^2)} \frac{\cos\theta_1}{\sqrt{\sin^2\theta_1 - N^2}} \end{aligned} \quad (4.1.9)$$

Here we make the following approximation:

$$\text{Arg} [e^{ik}] = \text{Arg} [\cos k + i \sin k]$$

Let  $k = 2i \frac{\Delta n}{n} \frac{N}{(1 - N^2)} \frac{\cos\theta_1}{\sqrt{\sin^2\theta_1 - N^2}}$ , which is a small imaginary quantity, so  $\cos k = 0$  and  $\sin k = k$ , which leads to  $\text{Arg} [e^{ik}] = ik = \text{Arg} [ik]$ . This way, the argument is eliminated, so we get:

$$\varphi_{EW} = \frac{\Delta n}{n} \frac{N}{(1-N^2)} \frac{\cos\theta_1}{\sqrt{\sin^2\theta_1 - N^2}} \quad (4.1.10)$$

### 4.1.3. Experimental process-Results

The maltodextrin and fructose samples were alternately injected in the flow cell and a trace was obtained for each direction of the magnetic field and light beam, respectively. The data traces are fit with the  $I_{CW}$  and  $I_{CCW}$  functions noted earlier, and the oscillation frequency is obtained. Each data point shown in fig.1 represents 4000 averaged laser shots. The magnetic field was reversed between each data point. After five consecutive data points were taken, the sample was cleaned by injecting plenty of water in the flow cell and substituted with the next sample in row. This way, it is ensured that the prism remains stable, and no jumps in the data are introduced. A sample of Glycerol, a non-chiral liquid material, is measured to serve as the background measurement. The background introduced using this method are very small, but it is comparable to the weak chirality signals of the samples. This is attributed mainly to the use of a multi-mode pulse laser: since there is no way to excite only one transverse mode inside the cavity, which would result in a perfectly defined spatial distribution of the laser energy, even a very small misalignment of the cavity optics can introduce a spurious effect, which would lead to a background comparable to the sensitivity of the instrument. Instead we used a multi-mode laser, where higher-order modes have very low energy, but many modes other than the lowest-order one are contributing, and hence the spatial distribution of the light beam inside the cavity is not well-defined.

The results of each channel are given in fig. 23 . The signal reversing process is shown in this figure. In Fig. 23a, the data points obtained for each magnetic field and light beam direction , while measuring a maltodextrin sample are explicitly shown. The data points represent the oscillation frequency extracted via fitting the trace, as noted before, and are taken every 2 minutes. The refractive index for these data points is 1.442. After applying the subtractions method discussed in paragraph 3.5., a  $\delta\omega$  is obtained for each data point, as in fig 23b. Doing so, the experimental data and comparison with theory are shown in fig 1.c. The data points in fig 23c are the average of 5 data points after the signal reversals, as in figure 23b.

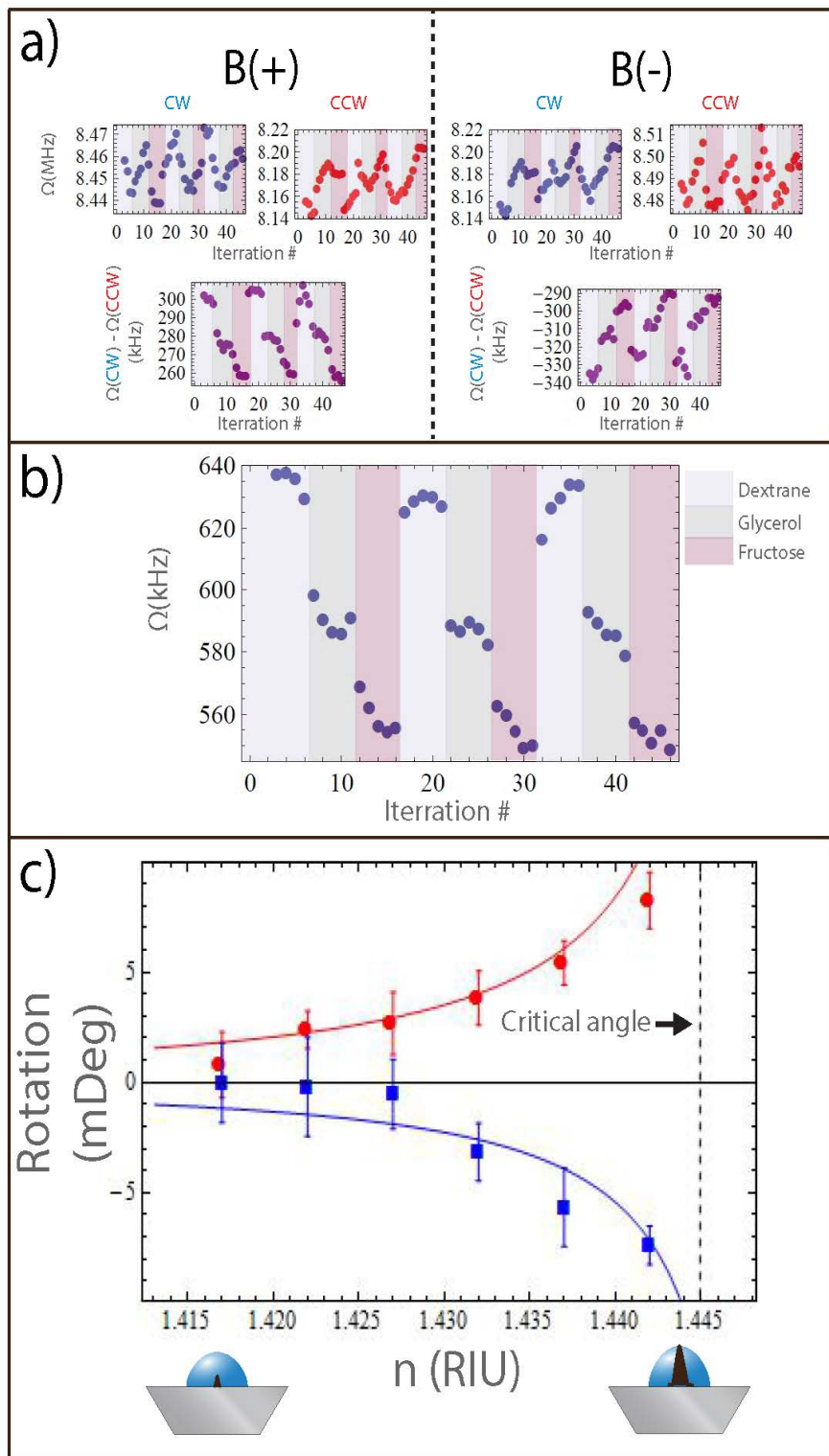


Figure 23: (a) The four oscillation frequencies,  $\omega_{CW+}$ ,  $\omega_{CW-}$ ,  $\omega_{CCW+}$ ,  $\omega_{CCW-}$  are shown for successive measurements of maltodextrin, glycerol and Fructose. (b) After the subtractions, the optical rotation of each solution is shown. (c) Measurements and theoretical predictions for  $n$  from 1.418 to 1.442. The error bars are  $2\sigma$  confidence intervals. (d) Evanescent wave forming inside the chiral medium.

#### 4.1.4. Discussion of the results

The data agree well with the theoretical predictions, as seen in fig.23c. The data, as well as the theory, show a sharp increase as  $N$  approaches to unity, so the effect is larger near index matching. This happens because, as the refractive indices of the chiral sample and the prism become closer, the angle of incidence is closer to the critical, so the Goos-Hänchen shift is larger, and the optical rotation induced is correspondingly larger. This is the case up to a certain refractive index though; near perfect index matching, the evanescent wave becomes larger than the chiral layer, and jumps on the other side of it, so the laser energy is partially transmitted, and the TIR conditions are no longer matched. The case of partial transmission can be explained in terms of the chiral slab configuration discussed earlier. The critical angle of incidence is larger than the angle of light incidence, so part of the beam is transmitted into the slab. Since the slab has a smaller refractive index than the substrate (the air,  $n \sim 1$ ), part of the beam is reflected at the slab-substrate interface and propagate back to the prism and part of it propagates to the substrate. As we move closer to index matching, the critical angle of incidence becomes larger, and therefore the TIR conditions are no longer matched, first at the prism-slab interface and then the slab-air interface. Eventually, when there is perfect index matching, the light is fully transmitted to the air.

## 5. Chirality measurement in thin films

### 5.1. Introduction

In this section, a possible configuration for the enhancement of the chiral signal of thin films is discussed. We are looking into the possibility of finding a way to enhance the chirality signal of a very thin layer of a material. First, we calculate the signal intensity for layers with thickness smaller than or equal to the light beam wavelength, in search for any amplification of the signal. Finally, a novel experimental setup, using a chiral etalon inside an optical cavity, is proposed and analysed, which is able to measure sensitively intensified chiral signals.

**Why thin chiral films?** Thin films are widely used in many applications in physics, chemistry, pharmacology and a number of other scientific fields. A practical advantage over bulk materials is that a thin film uses less substance for a measurement, which is



very helpful for a number of industrial sectors. One of the targets thus is reducing the substance needed to take a simple measurement of the chirality signal. The properties of a film with thickness comparable to a wavelength are also very different than the ones of a bulk material. Effects that take place in a thin layer when probed by a light beam such as resonance and interference can potentially enhance the measured signal or aid in other ways to obtain a measure of a weak effect which otherwise would not be possible to measure.

Here we discuss the possibility of the existence of any intensification of the chiral signal in a thin layer. The discussion made earlier about the evanescent wave forming and how it probes the chiral layer under measurement, pointed out that the optical rotation measured is induced at the evanescent wave. A larger evanescent wave results in a larger Goos-Hänchen shift, and a larger chirality signal measured. Thus, a layer thicker than the evanescent wave penetration depth is not introducing any larger rotation, provided that there are no effects such as waveguiding inside the layer. The penetration depth of the evanescent wave is in the order of half a wavelength up to a few wavelengths, when index matching occurs between the medium of incidence and the layer. Given that, it is expected that there will be a saturation value of the measured chiral signal after a certain layer thickness. What is to be confirmed is that the signal is linearly proportional to the layer thickness up to the saturation point, and there is no enhancement before that point. To do that, the optical rotation formula is used

$$\varphi_{EW} = \frac{1}{2} \text{Arg} \left[ \frac{r_{++}}{r_{--}} \right] \quad (5.1.1)$$

where  $r_{++}$ ,  $r_{--}$  are the previously noted reflection coefficients, using the helicity notation.

There are two general cases of a chiral slab configuration: one that induces waveguiding and one that does not. If the refractive index of the chiral slab is larger than the ones of the medium of incidence and substrate, the wave inserting the slab will reflect many times inside it as it propagates through it. Many reflections inside the slab result in a larger propagation length in the chiral medium, and thus a larger optical rotation. This configuration is characterised as an optically active Fabry-Perot interferometer, and was first proposed by Silvermann and Badoz<sup>[5]</sup> in 1994. On the other hand, if the refractive index of the chiral slab is lower than the one of the medium of incidence or the substrate, there will be either one or zero internal reflections inside the slab, and the configuration resembles to the one discussed in chapter 4. In this work, both cases are examined; the results are shown in section 5.3., after a brief discussion of the theory of the chiral Fabry-Perot interferometer.

### 5.2. Optically active Fabry-Perot interferometer

The discussion made in paragraph 2.6. pointed out that a light beam propagating through a chiral slab for which  $n_2 \leq n$  and  $n_1 \leq n$  can be trapped inside this chiral slab and internally reflect many times, after split in two beams, one of each circular polarization. This configuration is the optically active Fabry-Perot interferometer, which was introduced by Silvermann and Badoz [5], and analysed by Lalov and Miteva [3]. Here we examine this interferometer, which will be used in the next paragraph as the configuration for the search of any high chiral signals.

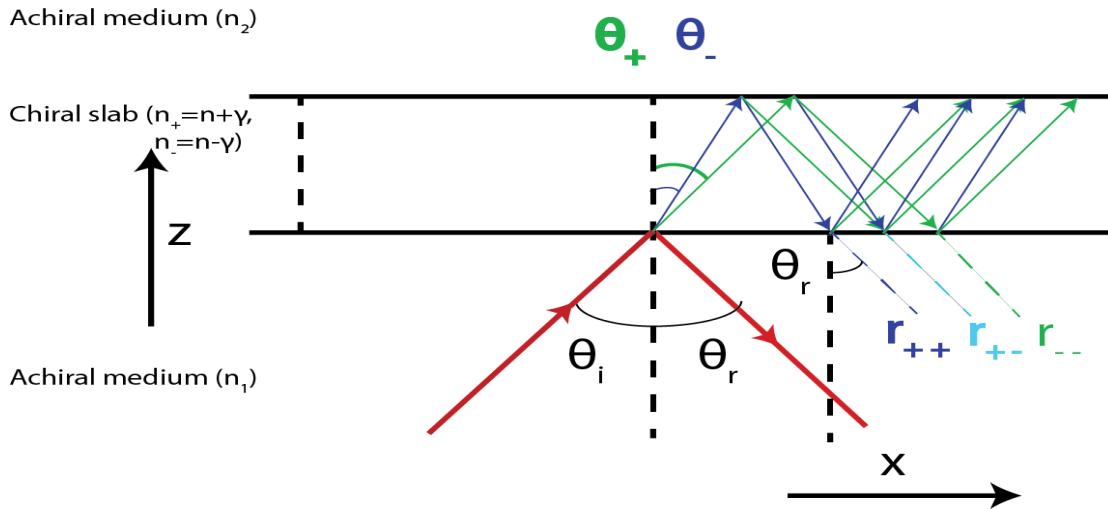


Figure 24: Multibeam interference from a chiral Fabry-Perot etalon

Consider an achiral Fabry-Perot interferometer. Figure 24 shows waveguiding, i.e. beam trapping in such an interferometer, and the corresponding reflected and transmitted beams. Multiple reflections of light inside the interferometer can be in or out of phase. The in-phase reflections create constructive interference, and the out-of-phase reflections create destructive interference. The phase difference between two successive reflected or transmitted beams is given by

$$\delta = \left(\frac{2\pi}{\lambda}\right) 2n l \cos\theta \tag{5.2.1}$$

The interference occurring at each point creates an interferometric spectrum (fig), with high peaks at the points where constructive interference occurs, and low valleys where destructive interference occurs. The distance between the high interferometric peaks is the Free Spectral Range (FSR) of the interferometer and is given by

$$\Delta\lambda = \frac{\lambda_0^2}{2n \lambda \cos\theta} \tag{5.2.2}$$

Or, in the frequency domain,

$$\Delta f = \frac{c}{2n l \cos\theta} \quad (5.2.3)$$

If the slab between the two media is optically active, there are some differences, owing to its double refractive index. Consider a p-polarized wave incident on the first chiral-achiral interface (see figure 24). Since the refractive index of the slab is higher than the one of the achiral medium, there will be a reflected-transmitted pair emerging from the reflection. Upon reflection at a chiral medium, the optical rotation induced at the evanescent wave formed alters the plane of the wave polarization. Thus the reflection gives rise to a perpendicular polarization component at the reflected beam, and  $E_r^{(0)} = (E_{rp}^{(0)}, E_{rs}^{(0)})$ , where

$$E_{rp}^{(0)} = R_p E_p \quad (5.2.4)$$

$$E_{rs}^{(0)} = -R_{ps} E_p \quad (5.2.5)$$

with  $R_p$  and  $R_{ps}$  being the Fresnel coefficients for the transmitted p-polarized component and the reflected s-polarized component (see appendix), respectively. Because of the ellipsometric phase shift introduced, the reflected wave polarization is elliptical. Inside the chiral slab, two waves of opposite circular polarizations are created, propagating towards the second chiral-achiral interface, labelled as b. Their electric field components are <sup>[3]</sup>

$$E_{+,-}^p, E_{+,-}^s = \mp i \operatorname{sgn}[\gamma] E_{+,-}^p \quad (5.2.6)$$

where

$$E_{+,-}^p = \frac{1}{2} (T_p \mp i \operatorname{sgn}(\gamma) R_{ps}) E_p \quad (5.2.7)$$

and  $T_p$  is again the Fresnel coefficient for the transmitted p-polarized component. These two waves reach the b interface with different phases, namely

$$\Delta_{\pm} = \frac{2\pi}{\lambda_0} d n_{\pm} \cos\theta_{\pm} = \frac{1}{2} (\Delta \pm \xi) \quad (5.2.8)$$

Where  $\Delta$  is the wave phase in the absence of chirality, given by 5.2.1 and  $\xi$  is the phase difference introduced because of the wave splitting

$$\xi = \frac{2\pi}{\lambda_0} \frac{|\gamma|d}{\cos\theta} \quad (5.2.9)$$

So the phase difference between the two waves is given by  $\Delta_+ - \Delta_- = \xi$ . This phase difference is produced after every reflection at a chiral-achiral boundary.

Upon reflection of a circularly polarized wave at oblique incidence, part of the light polarization is transformed to the opposite helicity. If reflection takes part inside a chiral medium, the effective refractive index of the two waves is different, so two reflected waves are created. Thus, for two waves reflected upon the interface b, four reflected waves are generated, propagating back towards the interface a. This internal reflection continues, up until the total wave energy is depleted, each time creating two reflected waves of opposite helicities for each incident wave. Part of the incident waves are transmitted over or under the slab, inducing constructive and destructive interference between them, as not all the waves are in-phase. After each internal reflection at the interface b,  $2^{2n}$  waves are transmitted over the slab, and  $2^{2n+1}$  waves are reflected back under the slab. The total reflection and transmission coefficients<sup>[6]</sup> are given in appendix, and will be simulated in the next section for the case of the optically active etalon.

### 5.3. Simulations

The first question one has to answer when thin films are to be used is “how thin?”. As noted before, when the evanescent wave is used as a probe, the film should be in the order of the wavelength, or, more precisely, in the order of the evanescent wave penetration depth. This is expected to be shown by simulating the optical rotation induced at TIR conditions versus the slab thickness; for a thickness much bigger than the evanescent wave height, the optical rotation should not be significantly higher than its value when the slab is of thickness comparable to that height. But, even considering an optically active etalon configuration, the slab should not be much thicker than the wavelength. The reason for that, as will be discussed later on, is that a ratio of  $d/\lambda \gg 1$  would introduce a large amount of losses too, which could result in a weak chiral signal measurement.

The first step in searching for any enhancement of the chiral asymmetries will be to

simulate, using 5.1.1, the chirality signal versus the layer thickness.

A prism made of fused silica ( $n_1=1.45332$ ) is to be used as the medium of incidence. Of course, other options exist, but for the simulations the same medium is used, to serve as a means of direct comparison of the theory and the measurements presented in the last chapter.

We first consider the exact refractive indices of the slab (maltodextrin,  $1.43 < n < 1.445$ ) and substrate (air,  $n_2=1$ ) which were used in the configuration shown at chapter 4. The slab is considered to be non-absorptive for the first simulations; this is not realistic, but is sufficient as a first approximation. Corrections in the simulations, which represent the absorption or any other losses (e.g. scattering because of non-parallel slab surfaces), will be introduced at a later stage.

Figure 25 shows the theoretical chiral signal versus the layer thickness, for various refractive indices of the slab up to 1.446. We saw that for  $n > 1.445$ , index matching conditions occur, the evanescent wave becomes very large and part of the wave is transmitted. This is why we set  $n > 1.445$  as a different case. This figure shows that for  $n < 1.445$ , the chiral signal is linearly proportional to the layer thickness up until a certain thickness, depending on the refractive index, and then it becomes saturated at a certain value, after which it is the same, no matter how thick the layer becomes. This is the expected result, and the reflection coefficients given here confirm it. The result shows that no enhancement is introduced in the chiral signal for very thin layers. For  $n=1.446$ , a positive second derivative appears, which needs to be examined. To do so, figure 26 shows the case of  $n_1 > n > 1.445$ . It shows that the positive second derivative observed in the previous figure does not go to infinity, but instead is the start of an interferometric spectrum. This spectrum displays much higher peaks than the measured signal from Sofikitis et al.. This result can be interpreted using the discussion of paragraph 5.2. For  $n > 1.445$ , the critical angle is larger than the angle of incidence, so a part of the wave is reflected into the slab. From there, for certain layer thicknesses, one or more internal reflections at the prism/slab interface will occur. This can indeed lead to waveguiding and an enhancement of the chiral signal. Thus the peaks observed in this plot are at the resonant layer thicknesses, i.e. the ones that, given a certain angle of incidence, can lead to as more reflections inside the chiral slab as possible. These peaks can be exploited for the measurement of a much intensified chiral rotation. To do so, an impractical way would be to try to control the slab thickness, until a peak in the optical rotation is crossed, and measure the signal there. But this is not experimentally feasible, as controlling the layer thickness with a sensitivity of some nanometers is technically impossible.

## Chirality measurement in thin films

*Figure 25: Optical rotation versus slab thickness , for  $\lambda=780$  nm and  $\theta_1 < \theta_c$*

*Figure 26: Optical rotation versus slab thickness , for  $\lambda=780$  nm and  $\theta_1 > \theta_c$  and  $n < n_1$*

## Chirality measurement in thin films

*Figure 27: Optical rotation versus slab thickness , for  $\lambda=780$  nm and and  $n > n_1$*

Before proposing a way to solve this problem, the case where  $n > n_1$  should be discussed. It is confirmed that, after a certain refractive index, there are peaks in the optical rotation vs layer thickness simulations, which are attributed to resonance. It is shown that, the higher the refractive index, the closer these peaks are to each other. This is the trademark of the Fabry-Perot interferometer; the peaks show constructive interference, and the distance between them should be an  $FSR = \frac{c}{2nl}$ . From this conclusion, we are motivated to alter the way of searching for enhancement: rather than simulating optical rotation in terms of layer thickness, we could do so in terms of wavelength.

Since waveguiding is a resonant phenomenon, the layer thickness where the peaks are displayed should be proportional to the wavelength. Considering this, a transformation from slab thickness to wavelength should be self-consistent; and controlling the wavelength is equivalent to controlling the thickness. It is much easier too, as scanning the laser wavelengths is easily feasible using a dye laser. The way this becomes possible will be shown in the next paragraph.

### Chirality measurement in thin films

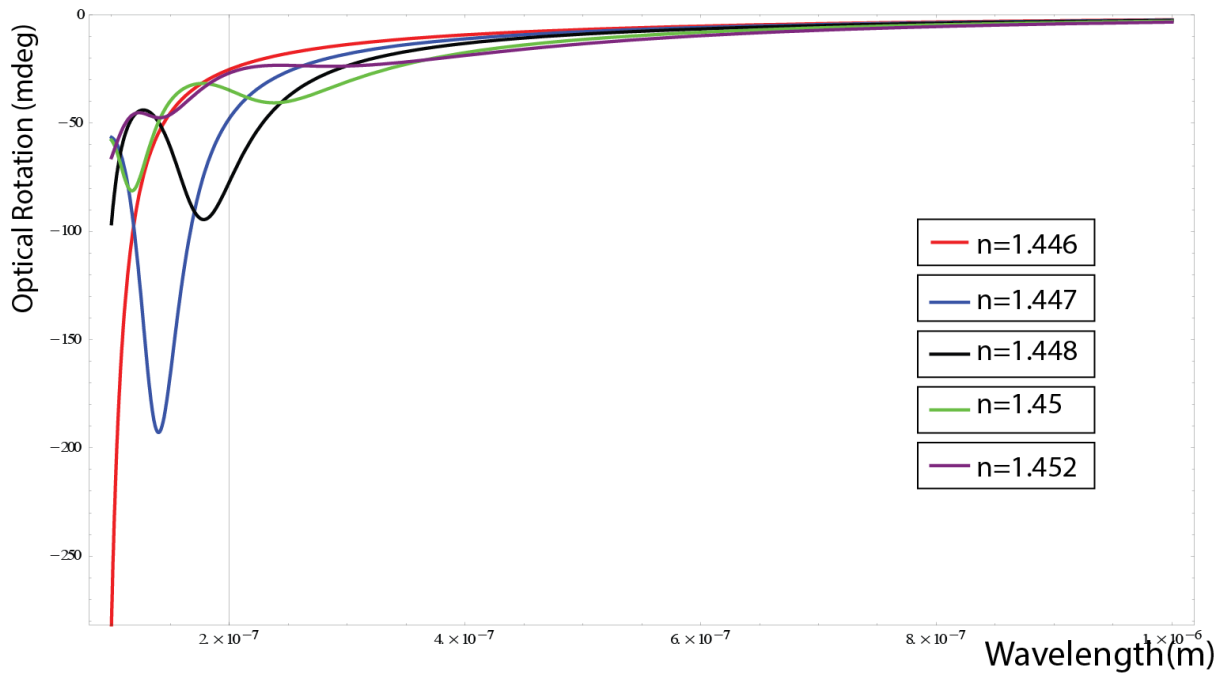


Figure 28: Optical rotation versus wavelength, for a slab with  $d=1 \mu\text{m}$  and  $\theta_i > \theta_c$

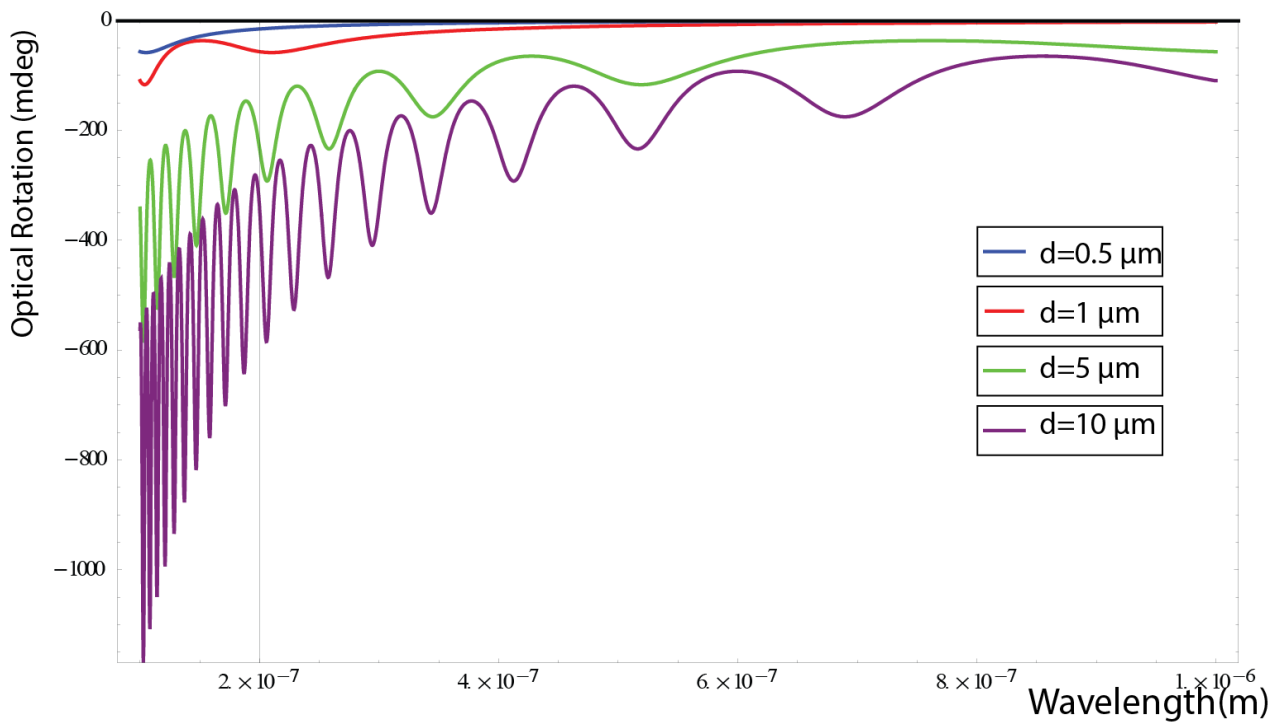


Figure 29: Optical rotation versus wavelength, for various slab thicknesses and  $n=1.449$



## Chirality measurement in thin films

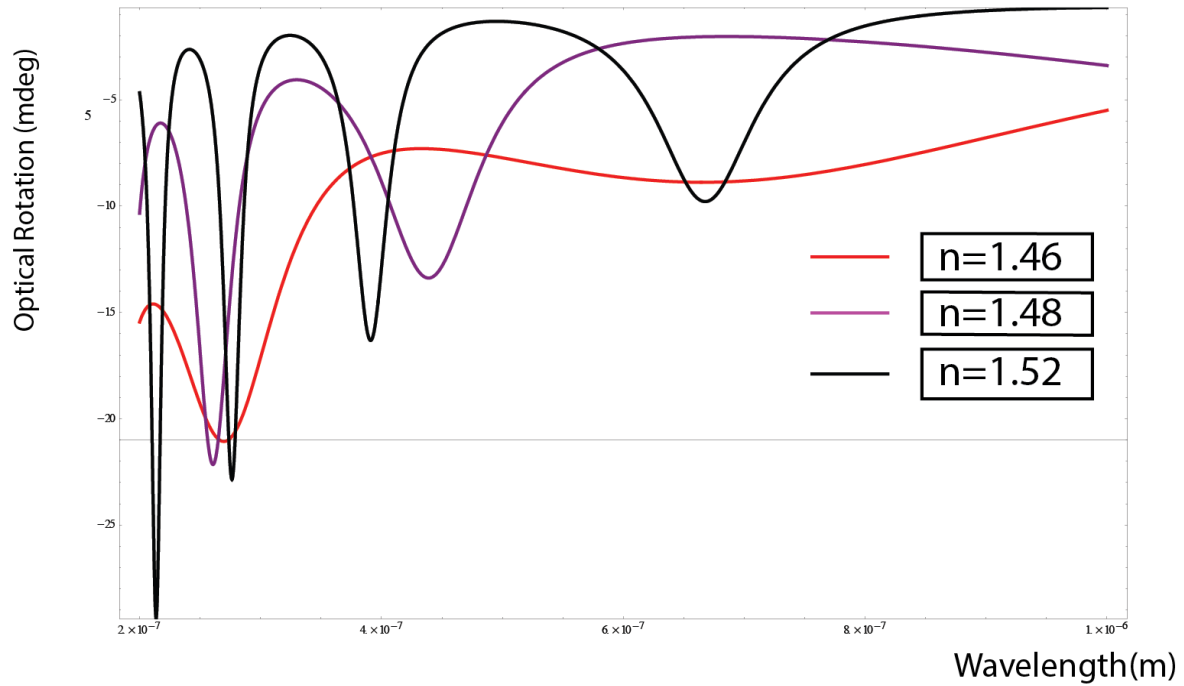


Figure 30 Optical Rotation versus wavelength, for  $d=1 \mu\text{m}$  and  $n > n_1$

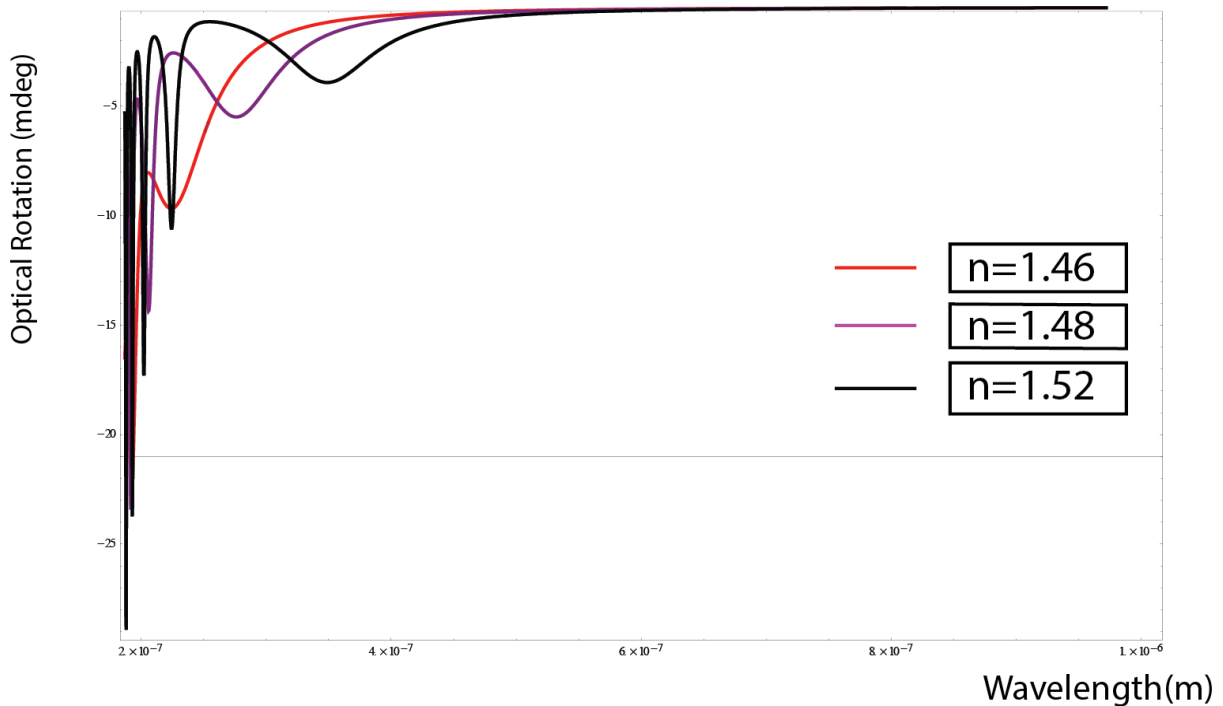


Figure 31: As above, but with the wavelength varying up to  $10 \mu\text{m}$ , so  $d/\lambda \ll 1$ . Notice that no interferometric peaks appear beyond  $\lambda \sim d$

The previous figures show a great optical rotation signal for matching prism and slab refractive indices. The only problem is, this enhancement occurs for  $d/\lambda \gg 1 \mu\text{m}$ .

The reason why this should be avoided will be shown later. In figures [25-26](#), this difference is pointed out. Both these figures demonstrate optical rotation versus wavelength, for  $d=1 \mu\text{m}$ . While in [figure 28](#) no interference peaks appear, except for low wavelengths, [figure 29](#) shows that a great optical rotation (up to 3 degrees) can be achieved if the layer thickness is greater than  $5 \mu\text{m}$ . As expected, the FSR of the interferometric spectrum is proportional to the layer thickness, which leads to more peaks for thicker layers.

For better understanding of the simulations, the etalon can be interpreted as a resonant cavity, where resonant modes are excited at certain given conditions. The peaks obtained at the simulations for certain wavelengths represent resonant modes of the light propagation inside the etalon. When such a mode is excited, the beam makes many passes back and forth through the etalon, thus undergoing a larger rotation of its polarization plane. Considering the ideal case of a non-absorptive etalon, a larger light path under any circumstances would induce larger optical rotation, thus giving a larger measurement signal. However, in the more realistic case of a non-ideal medium, where absorption and scattering would produce losses, larger optical path does not necessarily mean a better measurement.

The simulations shown before work well under two assumptions: a) that the etalon is non-absorptive, as discussed earlier and b) that the two interfaces are completely parallel, and the resulting reflected beams which interfere under the slab are completely parallel, and thus produce a perfect interferometric spectrum. Both these assumptions are of course unrealistic. If a more realistic picture is to be given, approximations should be introduced that represent these effects.

The case of an absorptive chiral etalon was examined by Lalov and Georgieva<sup>[4]</sup>. In this work, a term  $i \cdot n''$  is introduced as a first-order correction to the refractive index  $n$  of the chiral slab, to simulate the losses due to absorption. A realistic value for  $n''$  would be  $\sim 10^{-5}$ , which would represent all intrinsic losses due to the nature of the chiral slab. Lalov and Georgieva report large changes in the optical rotation, but their work considers very thick slabs ( $\frac{d}{\lambda} \approx 2000$ ), which is not the case for this work, where thin films are to be used. Figure 32 shows that there is no real change in the interference spectrum of an absorptive and a non-absorptive medium, up to a  $\frac{d}{\lambda}$  ratio of 60, if  $n''$  is at a realistic value ( $10^{-5}$ ). Thus absorption itself does not affect the optical rotation of light. However, in the next paragraph it will become clear that this is not the only parameter to be taken into account.

## Chirality measurement in thin films

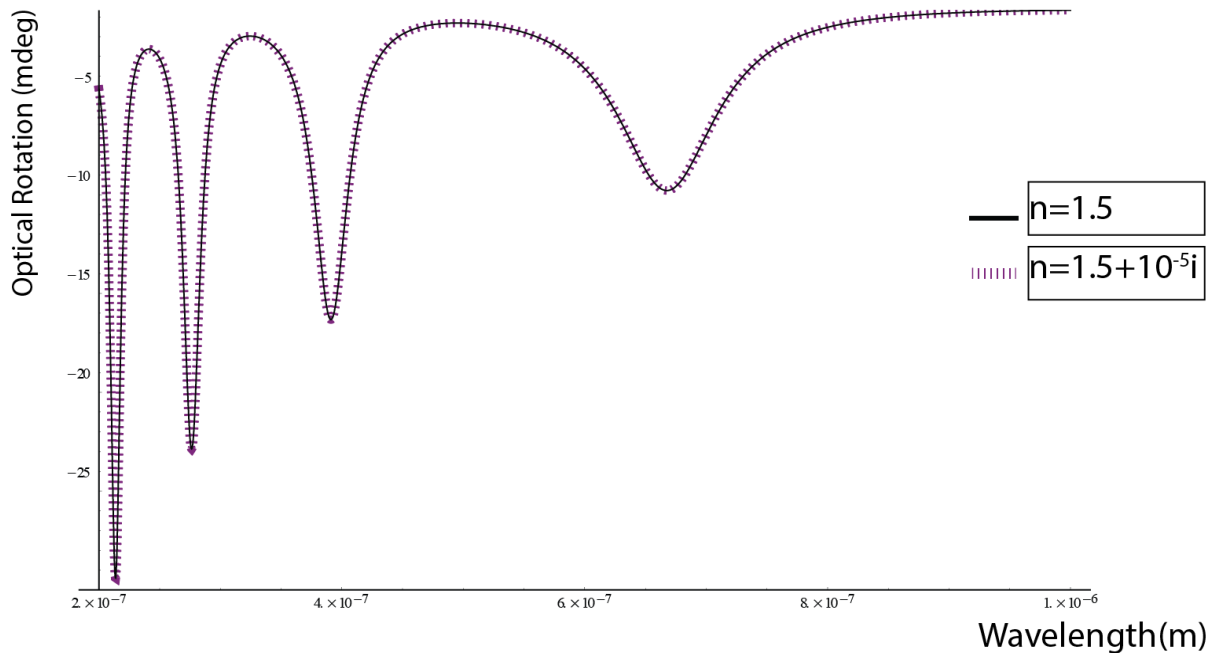


Figure 32: Interferometric spectrums of absorptive vs non-absorptive etalons of  $n=1.5$ .

The simulations shown before show the optical rotation of the reflected part of a beam of light propagating inside a chiral etalon. Apart from how large the optical rotation is, another important parameter of the experiment is the intensity of the reflected beam intensity, which is not examined by the simulations already presented.

The chiral etalon, as noted before, can be seen as a resonant cavity, with reflectivities which depend on the refractive indices of the non-chiral materials. A high-finesse chiral etalon would produce more intracavity reflections at resonance, resulting in a larger effective pathlength, hence a larger optical rotation signal. If, though, the cavity is low-finesse, high losses will occur with every reflection at the slab-substrate interface. Since the technique intended to be used in this work is cavity-enhanced, the quality of the measurement depends strongly on a high number of passes through the mirror cavity. High losses owing to transmission from the slab to the substrate would then undermine the ability of the configuration to produce an accurate and sensitive measurement. To avoid this, the losses because of transmission on the other side of the slab should be mapped, as in figure 33. In this figure, the net reflectance ratio of the light beam is examined, for high and low slab thickness to wavelength ratios, with and without taking into consideration the absorption inside the slab. The refractive index used is moderately high, but realistic for a liquid(1.6), the angle of incidence is  $84^\circ$  and  $n''=10^{-5}$ . For the  $\frac{d}{\lambda}$  ratios at which resonance occurs, the large amount of passes inside the etalon give rise to a higher amount of losses because of transmission to the substrate. This is depicted by the reflectance valleys at certain points of the graph. For

## Chirality measurement in thin films

low  $\frac{d}{\lambda}$  ratios, the reflectance is very high, with only 0.6% losses for a slab 2.5 times the wavelength. This is a losses level that can be afforded by a mirror cavity, assuming a mirror reflectivity  $\sim 0.99$ . If, though, the simulation is expanded up to  $\frac{d}{\lambda}$  ratios much bigger than unity, the losses at the resonant modes escalate up to a few percent. Note that the losses shown are the net losses after the waveguiding, not the losses per pass inside the etalon. That high losses can result in the loss of the whole light energy after 20-30 passes inside the chiral etalon, which is too small a number for a high-sensitivity experiment. An acceptable level of transmission losses would be around the respective cavity mirror losses; any more than that would restrict the number of passes to much less than  $\sim 100$ , which are needed for the desired measurement sensitivity to be achieved.

*Figure 33: Reflectances for s(a,b) and p(c,d) polarization incident, for a ratio  $\frac{d}{\lambda}$  up to 3 and 20.*

To calculate the passes that can be achieved through the cavity, the mirror and etalon reflectivities should be known. Then the number of passes is derived by the following calculations:

$$(R_{et} * (R_m)^4)^N = 0.01 \Rightarrow N = \log_{R_{et} * R_m} (0.01) \quad (5.3.1)$$

Where  $R_{et}$  is the etalon reflectivity,  $R_m$  is the mirror reflectivity, exponentiated to 4, as it is assumed that the cavity will be designed in the same way as in Bougas et al.<sup>[1]</sup> and N is the number of passes. The term 0.01 is introduced as a measure of the point in which the laser pulse will have almost totally escaped the cavity. Using this formula for the conditions examined in figure 33, and assuming  $\frac{d}{\lambda} \approx 2.5$ , which corresponds to  $R_{et}=0.994$ , and  $R_m=0.995$ ,  $N \sim 175$ . This is an acceptable number of passes, which can provide a sensitive measurement of the chirality factor  $\gamma$ .

#### **5.4. Experiment proposal**

The discussion made earlier provides the necessary knowledge for the design of a configuration that can sensitively measure the chiral factor  $\gamma$  of a chiral slab. In this paragraph, a number of possible configurations for this experiment are proposed.

For the measurement of chirality signal, a running cavity configuration is needed, as noted in paragraph 3.4. There are certain advantages and disadvantages in the use of either a triangular or bow-tie cavity. While a bowtie cavity is easier to construct, a triangular cavity, with a prism serving as a reflecting surface, serves in that it allows the measurement of much lower refractive index. This is because the angle of incidence at the etalon is lower, hence the light is transmitted to the etalon for lower etalon refractive indices, while the TIR conditions of the medium of incidence-slab-substrate configuration are retained. Apart from the higher variety on samples that can be measured, the use of lower refractive index samples aids in that these samples are much easier to be created. A waveplate compensator should be used inside the cavity, to compensate for the phase shifts induced by the reflections at the mirrors and other spurious birefringences that exist, and are not cleared by the signal reversals.

In section 4.4, the experimental process, as well as the data acquiring and data fitting processes are discussed. The final experimental data showed the measured optical rotation versus the refractive index, for different refractive indices of the same sample. Here, this process shall be different. The measurements of optical rotation will be with respect to the laser wavelength. Since the laser wavelength is to be very precisely determined, a tunable dye laser can be used to control the wavelength of the laser, which will probe the chiral etalon. These lasers have extremely narrow bandwidth, at the order of a few parts in a thousand wavenumbers, and can be tuned in a wide range of very precisely determined wavelengths. The measurements of the induced optical rotation will be obtained in the same way as in Sofikitis et al., only for

different wavelength values. These values are to be compared with the theoretical values of the optical rotation versus the wavelength, using a mathematical model. The confirmation of the theoretical values for known slab thickness, refractive indices and wavelength should provide a proof of principle for the ability of this configuration to measure the chiral effect  $\gamma$  of a thin chiral film.

In the previous paragraph, a discussion was made about the optimal number of passes through the cavity, for larger amplification of the chiral signal measured. As shown before, a high number of passes could be produced by setting the  $\frac{d}{\lambda}$  ratio close to unity, hence avoiding high losses per pass through the etalon due to absorption. A low  $\frac{d}{\lambda}$  ratio can result in about a hundred passes through the cavity, whereas a ratio of around 10 allows a few tens of passes. In the latter case, though, since the effective pathlength is higher, the optical rotation induced is much larger. If such a ratio is to be chosen, the lower number of passes would theoretically be compensated by the large optical rotation per pass. That given, both cases should be examined, since any spurious experimental effects could give an advantage in one or the other method.

## 6. Bibliography

### Bibliography

- 1: L. Bougas, G. E. Katsoprinakis, W. von Klitzing, J. Sapirstein, and T. P. Rakitzis, *Cavity-Enhanced Parity-Nonconserving Optical Rotation in Metastable Xe and Hg*, *Physical Review Letters*, 2012
- 2: Dimitris Sofikitis, Lykourgos Bougas, Georgios E. Katsoprinakis, Alexandros K. Spiliotis, Benoit Loppinet and T. Peter Rakitzis, *Evanescent-wave and open-air chiral sensing via signal-reversing cavity-enhanced polarimetry*, *Nature*, 2014
- 3: I.J.Lalov and A.I.Miteva, *Optically Active Fabry-Perot Etalon*, *Journal of modern Optics*, 2007
- 4: I.J.Lalov and E.M.Georgieva, *Optically Active Absorptive Fabry-Pérot Etalon*, *Journal of modern Optics*,
- 5: M.P.Silvermann and J.Badoz, *Interferometric enhancement of chiral asymmetries: ellipsometry with an optically active Fabry-Perot interferometer*, 1993
- 6: J. Lekner, *Optical properties of isotropic chiral media*, *Pure Applied Optics*, 1996
- 7: F. Goos and H. Hänchen, *Ein neuer und fundamentaler Versuch zur Totalreflexion*, *Annalen der Physik*, 1947

## Bibliography

- 8: A.Ghosh and P.Fisher, *Chiral Molecules Split Light: Reflection and Refraction in a Chiral Liquid*, *Physical Review Letters*,2006
- 9: A.O'Keefe, D.A.G.Deacon, *Cavity ring-down optical spectrometer for absorption measurements using pulsed laser sources*, *Review of Scientific Instruments*,1988
- 10: A.Karaiskou,V.Papadakis, B.Loppinet, T.P.Rakitzis, *Cavity ring-down ellipsometry*, *The Journal of Chemical Physics*,2009
- 11: M.Everest, V.Papadakis, K.Stamataki, S.Tzortzakis, B.Loppinet, T.P.Rakitzis, *Evanescent-Wave Cavity Ring-Down Ellipsometry*, *The Journal of Physical Chemistry Letters*,2011
- 12: Katerina Stamataki, Vassilis Papadakis, Michael A. Everest,Stelios Tzortzakis,Benoit Loppinet, and T. Peter Rakitzis, *Monitoring adsorption and sedimentation usingevanescent-wave cavity ringdown ellipsometry*, *Applied Optics*,2013
- 13: V. Evtuhov and A. E. Siegman, *A "Twisted-Mode" Technique for Obtaining Axially Uniform Energy Density in a Laser Cavity*, *Applied Optics*,1965
- 14: A.Kastler, *Champ lumineux stationnaire à structure hélicoïdale dans une cavité laser*, *Comptes Rendus de l'Académie des Sciences Paris B*,1970
- 15: T. Muller, K. B. Wiberg, and P. H. Vaccaro, *Cavity Ring-Down Polarimetry (CRDP): A New Scheme for Probing CircularBirefringence and Circular Dichroism in the Gas Phase*, *Journal of Physical Chemistry A*,2000
- 16: T. Muller, K. B. Wiberg, and P. H. Vaccaro, *Cavity ring-down polarimetry (CRDP): theoreticaland experimental characterization*, *Journal of the Optical Society of America*,2002
- 17: Scholarpedia, *Goos-Hänchen Shift in Optical Total Internal Reflection*, [http://www.scholarpedia.org/article/Goos-H%C3%A4nchen\\_effect#Goos-H.C3.A4nchen\\_Shift\\_in\\_Optical\\_Total\\_Internal\\_Reflection](http://www.scholarpedia.org/article/Goos-H%C3%A4nchen_effect#Goos-H.C3.A4nchen_Shift_in_Optical_Total_Internal_Reflection),

## 7. Appendix-Reflection coefficients

The general formulae for reflection amplitudes, which characterize the optical properties of a chiral layer with two refractive indices,  $n_{\pm}$ , are given by Lekner<sup>[6]</sup>. Medium 1 is the medium of incidence and medium 2 is the substrate.

$$Dr_{ss} = G_1 F_2^+ + 8c_1 c_2 c_+ c_- (m^2 + 1)(m'^2 - 1) Z_+ Z_- - g_1^+ f_2^- Z_+^2 - g_1^- f_2^+ Z_-^2 + G_1^+ F_2^- Z_+^2 Z_-^2$$

$$Dr_{pp} = -(G_1^+ F_2^- + 8c_1 c_2 c_+ c_- (m^2 + 1)(m'^2 - 1) Z_+ Z_- - g_1^- f_2^+ Z_+^2 - g_1^+ f_2^- Z_-^2 + G_1^- F_2^+ Z_+^2 Z_-^2)$$

$$Dr_{sp} = Dr_{ps} = -2imc_1 \{ (c_+ - c_-) [F_2^+ - F_2^- Z_+^2 Z_-^2] + (c_+ + c_-) [f_2^- Z_+^2 - f_2^+ Z_-^2] \}$$

where

$$m = n/n_1,$$

$$m' = n/n_2,$$

$$c_{\pm} = \cos\theta_{\pm},$$

## Appendix-Reflection coefficients

$$c_{\pm} = \cos\theta_{\pm}$$

D is a common denominator, given by

$$D = F_1^+ F_2^+ - 8c_1 c_2 c_+ c_- (m^2 - 1)(m'^2 - 1) Z_+ Z_- - f_1^- f_2^- Z_+^2 - f_1^+ f_2^+ Z_-^2 + F_1^- F_2^- Z_+^2 Z_-^2,$$

$Z_{\pm}^{\pm} = e^{iq_{\pm}d}$ , which gives the phase increments in a single transit of the slab for the two helicities,

and

$$F_1^{\pm} = 2m(c_1^2 + c_+ c_-) \pm (m^2 + 1)(c_+ + c_-)c_1$$

$$F_2^{\pm} = 2m'(c_2^2 + c_+ c_-) \pm (m'^2 + 1)(c_+ + c_-)c_2$$

$$G_1^{\pm} = 2m(c_1^2 - c_+ c_-) \pm (m^2 - 1)(c_+ + c_-)c_1$$

$$G_2^{\pm} = 2m'(c_2^2 - c_+ c_-) \pm (m'^2 - 1)(c_+ + c_-)c_2$$

$$f_1^{\pm} = 2m(c_1^2 - c_+ c_-) \pm (m^2 + 1)(c_+ - c_-)c_1$$

$$f_2^{\pm} = 2m'(c_2^2 - c_+ c_-) \pm (m'^2 - 1)(c_+ - c_-)c_2$$

$$g_1^{\pm} = 2m(c_1^2 + c_+ c_-) \pm (m^2 + 1)(c_+ - c_-)c_1$$

$$g_2^{\pm} = 2m'(c_2^2 + c_+ c_-) \pm (m'^2 - 1)(c_+ - c_-)c_2$$